Conservation of spatiotemporal DNA replication origin and terminus segregation patterns in *Sinorhizobium meliloti* with re-engineered bi- and monopartite genomes

Marcel Wagner[1,2], Johannes Döhlemann[1,2], David Geisel[3], Patrick Sobetzko[1], Javier Serrania[1,2], Peter Lenz[1,3] and Anke Becker[1,2]*

[1]Center for Synthetic Microbiology (SYNMIKRO), Marburg, Germany

[2]Department of Biology, Philipps-Universität Marburg, Marburg, Germany

[3]Department of Physics, Philipps-Universität Marburg, Marburg, Germany

Keywords: *Sinorhizobium meliloti*, genome restructuring, replicon fusion, multi-replication origin chromosome, spatiotemporal dynamics of genomic loci

*Correspondence: anke.becker@synmikro.uni-marburg.de

■ ABSTRACT

While the vast majority of bacterial genomic DNA molecules contain a single origin of replication, some natural isolates and engineered strains were reported to contain chromosomes derived from cointegration events of multiple replicons. We investigated effects of multiple DNA replication origins and terminus regions on spatial DNA organization and spatiotemporal replicon segregation in the alphaproteobacterium *Sinorhizobium meliloti*. Strains with a bi- and monopartite genome configuration were constructed by Cre/*lox*-mediated site-specific fusions of the secondary replicons pSymA and pSymB, and of the chromosome, pSymA and pSymB. The design of these strains maintained replichore ratios, GC skew, as well as distribution and orientation of KOPS and coding sequences. Growth of these strains was essentially unaffected, except for high salt conditions. Replication initiation at the three origins as well as key features of spatial organization and spatiotemporal segregation were maintained in the triple-replicon fusion strain. Cell growth was slowed down by deleting, either individually or together, the pSymA- and pSymB-derived replication initiator encoding *repC* genes with their intrinsic origin of replication from the dual or triple replicon cointegrates, respectively. Replication of the triple cointegrate, characterized by the chromosomal *oriC* as sole origin and a strongly disbalanced replichore ratio, terminated in the original chromosomal *terC* region, suggesting a replication trap. Progression of replication of the longer replichore was not blocked but impaired, possibly due to the retained secondary replicon's terminus regions and reverse alignment of replichore-orienting sequence features following from the deletion of replication origins. Moreover, during the cell cycle of this strain, *oriC* aberrantly localized and served as replication initiation site in the mid cell area of the cell with the oldest cell pole. Growth deficiency of this strain was attenuated by a suppressor mutation causing amino acid substitution R436H in the cell cycle histidine kinase CckA.

■ AUTHOR SUMMARY

To proliferate, any cell must reliably replicate its genomic DNA and allocate copies to the future cell compartments prior to cell division. While eukaryotic cells typically use multiple origins of replication per chromosome to initiate replication, bacteria usually rely on a single origin of replication per genomic DNA

molecule. About 10 % of total-genome-sequenced bacterial species maintain multipartite genomes. Derivatives of such bacterial species with fused genomic DNA molecules − either natural bacterial isolates or engineered strains − demonstrate that bacteria can handle genomic DNA molecules with multiple origins of replication in their cell cycle. In our study we show that a cointegrate of three genomic replicons maintains key features of spatial organization and segregation dynamics of each replicon in the alphaproteobacterium *Sinorhizobium meliloti*. The spatial association of origin and terminus regions to specific cell areas, as well as preserving typical features of bacterial genome organization, such as replichore ratio and the distribution and DNA strand specificity of coding sequences and replichore-orienting sequence motifs, are likely key to maintaining genomic cointegrates with multiple replication origins in a bacterial cell without major loss of cell fitness.

■ INTRODUCTION

About 10 % of the whole genome-sequenced bacterial species represented in databases maintain multipartite genomic DNA [1]. Their genome architectures are diverse in terms of number and size of DNA molecules maintained. In addition to the main chromosome, these bacteria harbor one or more large secondary replicons classified as secondary chromosomes, chromids or megaplasmids according to origin type, gene content, and size [1,2].

In contrast to chromosomes of eukaryotes and archaea that commonly have multiple origins of replication, bidirectional replication of bacterial main chromosomes is usually initiated at a single origin of replication (*ori*) and finishes in a termination zone (*ter*) when converging replication forks meet [3-5]. Nonetheless, several reports support that DNA molecules with more than one origin of replication can be maintained in bacteria. Strand asymmetry patterns suggest multiple origins of replication in genomes of the γ-proteobacterial endosymbiont *Wigglesworthia glossinidia* and the cyanobacterium *Synechocystis* 6803 [6]. DNA molecules with two or three origins of replication, which originated from cointegration events of two or three replicons, were reported for natural strain isolates of the γ-proteobacterium *Vibrio cholerae* and the α-proteobacterium *Sinorhizobium meliloti*, respectively [7-9]. Further evidence for the possibility

of maintaining a chromosome with multiple origins of replication derives from engineered chromosomes of the γ-proteobacterium *Escherichia coli* that in addition to the native *oriC* locus carry one or two extra copies of this origin of replication [11,12].

In bacterial cells, the genomic DNA is highly organized, and replication and segregation are coordinated in space and time [13]. Common patterns in rod-shaped cells are longitudinal arrangement of the main chromosome with the origin of replication at the old cell pole and the terminus region at the new cell pole (*ori*-*ter*), or transverse arrangement (left-*ori*-right) placing the two replichores in the left and right halves of the cell. The former is e.g. characteristic of *V. cholerae* and the α-proteobacteria *Caulobacter crescentus*, *S. meliloti* and *Brucella abortus*, and the latter of slow-growing *E. coli* [14-16]. In *B. abortus* harboring a main chromosome and a chromid, and in *S. meliloti* possessing a main chromosome, a chromid and a megaplasmid, the *ori*s of the secondary replicons localize subpolar to the old cell pole in newborn cells [16-18]. This spatial arrangement differs from that of the chromid (Chr II) in *V. cholerae*. Here, in G_1-phase cells, the *ori* of Chr II localizes at midcell and its *ter* closer to the cell's new pole [19]. In *V. cholerae* and *S. meliloti*, it was shown that segregation of the replicons follows a predominant order, with segregation of the *ori* of the main chromosome preceding that of the secondary replicon(s) [18,20].

This raises questions about the effects of multiple *ori*s and *ter*s in cointegrated replicons on spatial DNA organization and spatiotemporal patterns of replicon segregation. In this study, we addressed these questions in *S. meliloti* Rm1021, which carries the main chromosome (3.65 Mbp), megaplasmid pSymA (1.35 Mbp) and chromid pSymB (1.68 Mbp) [21]. Vertical transmission of the secondary replicons is mediated by replicon-specific *repABC* loci [22] that provide a complete replication and segregation system [18]. Beside the DNA replication initiator protein RepC, the *repABC* operon encodes the ParAB-type partitioning proteins RepAB. Together with centromer-like sequences (*parS*) these proteins are crucial for segregation of replicated DNA [23]. In contrast to the chromosomal origin (*oriC*) characterized by specific elements including DnaA-boxes and DNA unwinding elements (DUE) [5], the origins of *repABC*-type secondary replicons (*oriV*) are located within an AT rich region of RepC [24].

In this study, we constructed *S. meliloti* strains with a bi- and monopartite genome configuration with multiple *ori*s or a single *ori* per genomic DNA molecule. We show that a cointegrate of three genomic replicons that per design preserved typical features of bacterial genome organization, such as replichore ratio, and distribution and orientation of coding sequences and replichore-orienting sequence elements, maintained key features of spatial organization and segregation dynamics of each replicon. Furthermore, we show that an engineered strain with monopartite genome configuration, harboring *oriC* as sole origin of replication and characterized by a strongly unbalanced replichore ratio is viable, but impaired in growth. We report evidence for replication termination in the original *terC* region in this strain and that this engineered genome configuration affects polar localization of *oriC* and replication progression. A suppressor mutation in the cell cycle histidine kinase CckA was identified that likely attenuates growth deficiency of this strain.

■ RESULTS

Replicon fusions preserving strand asymmetry patterns

To study the properties of a triple-replication origin chromosome in *S. meliloti* in terms of spatial organization and spatiotemporal dynamics as well as propagation stability during the cell cycle, we merged the tripartite genome of this α-proteobacterium into a single DNA molecule. Targeted fusions of the three replicons were achieved by Cre/*lox*-mediated recombination in *S. meliloti* SmCreΔhsdR [25]. This strain, further referred to as wild type in this study, lacks *hsdR* encoding a restriction endonuclease and carries chromosomally integrated *cre* encoding Cre recombinase. This recombinase catalyzes site-specific recombination of DNA between *loxP* sites. Replicon cointegrations sporadically occurring in *S. meliloti* by recombination between *nodPQ1* and *nodPQ2* as well as between the *algI* paralogues *SMb20843* and *SMc01551* [7] acted as blueprint for selection of the fusion sites.

Following integration of *lox* sites, in close proximity to *nodPQ1* and *nodPQ2*, megaplasmid pSymA and chromid pSymB were initially merged to generate pSymAB by induced Cre/*lox*-mediated site-specific recombination. Thus, the resulting strain SmAB harbored a bipartite genome composed of the main

chromosome and pSymAB (Fig 1A; S1 Fig). Following integration of a *lox* site in vicinity to both *algI* paralogues on chromosome and pSymAB, and induced Cre/*lox*-mediated site-specific recombination, these genomic elements were merged, giving rise to a single genomic DNA molecule in strain SmABC (Fig 1A, S1 Fig). To reduce the possibility of direct revertants after the A-B and AB-C fusion steps, we locked the genomic design by deletion of the remaining active *lox* site on both the AB and ABC fused replicons. This deletion was achieved by homologous recombination between the paralogous *nodPQ* and *algI* genes flanking each of these *lox* sites, respectively (S1 Fig). Thus, in SmAB and SmABC, the AB and ABC DNA molecules each contained only one remaining inactive lox site with downstream antibiotic resistance marker. Fusion sites, correct genomic arrangements, and genome sequence of SmAB and SmABC were validated using PCR (S2 Fig), Pulsed-field gel electrophoresis (PFGE) (Fig 1B), and Illumina paired-end sequencing, respectively.

SmAB and SmABC genomic DNA configurations were designed to display wild type-like replichore ratios and distribution of GC content (Fig 1A; S3 and S4 Fig). Replichore orientation was reported to be defined by factors such as KOPS (FtsK orienting polar sequence) motifs and orientation of strongly expressed genes, both mostly situated on the leading DNA strand [26-28]. Each of the *S. meliloti* replichores contains a higher number of protein-coding genes on the leading than on the lagging strand (S5 Fig). This bias was preserved in SmAB and SmABC, even though two and three of the six replichores, respectively, were composed of segments originating from two or three different replicons of the wild type (Fig 1C). Also, the distribution of sequence motifs matching the *E. coli* KOPS consensus reflected the replicon structure and showed a strand asymmetry pattern with increasing motif density from *ori* towards *ter* in the replicons of wild type, SmAB and SmABC (Fig 1D; S6 Fig).

Cell growth and morphology were not affected by the genome rearrangements

Like other α-proteobacteria, *S. meliloti* undergoes asymmetric cell division which leads to siblings of uneven cell size [18,29,30]. Cell shape and size of the *S. meliloti* replicon fusion strains and the wild type were indistinguishable by microscopic analysis (Fig 2A). A few cells with strongly asymmetrically placed

137 constriction sites, probably resulting in minicells after cell division, were observed in cultures of the
138 *S. meliloti* wild type, SmAB and SmABC strains in TY (complex) and high salt TY media (S7A Fig). A
139 quantitative analysis identified a maximum of about 0.3 % minicells in wild type and replicon fusion strain
140 cultures (S7B and S7C Fig). Because of the very low number of minicells in the cell populations, clear
141 differences in the percentage of minicells in cultures of these strains in both media is not evident. When
142 cultivated in TY or low phosphate minimal MOPS (defined) media, cell growth of both replicon fusion
143 strains was similar to that of the wild type (Fig 2B). To analyze the effect of high-salinity and hyperosmotic
144 stress on these strains, TY medium was supplemented with 0.4 M NaCl and 0.5 M sucrose, respectively.
145 Compared to the wild type, SmAB and SmABC appeared only slightly impaired in growth in these media
146 (Fig 2B). Supplementing TY medium with 0.6 M NaCl or 0.7 M sucrose enhanced the difference in growth
147 between wild type and replicon fusion strains (S8B Fig).

148 **Origins of secondary replicons became expendable in the strain with monopartite genome**
149 **configuration**

150 We asked if a single replication origin would be sufficient for proper vertical transmission of the AB and
151 ABC DNA molecules in SmAB or SmABC. We attempted to inactivate *oriC* by deletion of various DNA
152 fragments in the annotated *oriC* region including putative DnaA boxes [31] (S9 Fig). However, our efforts
153 to delete these DNA regions were not successful. Further, we aimed to inactivate *oriA* and *oriB* individually
154 in the wild type and SmAB, and individually or together in SmABC. To this end, the *repB-repC* intergenic
155 region and the *repC* coding region (*repC2* of pSymA and *repC1* of pSymB) were targeted for deletion
156 (S10A Fig). In the wild type, deletion of these *repC* regions was not achieved. However, SmAB or SmABC
157 lacking either of these regions (SmABΔrepC1, SmABΔrepC2 or SmABCΔrepC1, SmABCΔrepC2) or
158 SmABC lacking both these regions (SmABCΔoriV) were obtained (S10B Fig). The configuration of the
159 genomic DNA in all these strains was validated by PFGE (S10C Fig). Illumina sequencing verified the
160 intended genetic changes in SmAB, SmABC and SmABCΔoriV, and revealed modifications resulting from
161 the construction process (S6 and S7 Table). Apart from these modifications, we identified only up to three

single nucleotide variations (SNVs) per engineered genome compared to the wild type genome (S8 Table), which we suppose are unlikely to be relevant to bacterial strain survival or fitness.

The sequential inactivation of the secondary replicon *oriV*s was associated with a gradually increasing growth defect, which appeared to correlate with the number of *oriV*s per DNA molecule. Deletion of a single *repC* copy in SmAB resulted in a more severe growth defect than in SmABC, whose monopartite genomic DNA still carried two replication origins (*repC* and *oriC*) after deletion of one *repC*. However, deletion of both *repC* copies in SmABC caused the most severe growth defect (Fig 3A), even though cell morphology was inconspicuous in snap shot analysis (Fig 3B).

To test if replication is initiated at all three *ori*s and to determine the replication termination regions of the triple replicon fusion molecule in SmABC a Marker Frequency Analysis (MFA) was performed. The MFA data indicate that all three *ori*s mediated bidirectional replication (Fig 3C; S11B Fig). Furthermore, this data suggests that replication terminated in regions close to or overlapping the MFA minima for chromosome, pSymA and pSymB identified in the parental strain with tripartite genome configuration (S11A Fig), which roughly match with predicted *ter* regions [32]. MFA analysis of SmABCΔoriV shows clear sequence read enrichment with a maximum at *oriC* but no additional enrichment maxima at the mutated *repABΔC* (Δ*oriA*/Δ*oriB*) regions. The latter suggests loss of function of *oriA* and *oriB* in SmABCΔoriV when compared to SmABC (Fig 3C). This analysis also suggests replication termination in a region close to or overlapping *terC*, which separates two replichores largely differing in size with a ratio of approximately 3:1. (S11C Fig). Plateaus or decrease in locus frequencies, including Δ*oriB*, *terB* and *terA* regions, might indicate replication obstacles in the single-replicon monopartite genomic DNA. In addition, fluorescence microscopy-based analysis of mCherry-fused DNA polymerase III beta subunit DnaN over the cell cycle revealed a maximum of two fluorescent foci in cells with monopartite genomic DNA containing *oriC* as sole replication origin in contrast to four to five foci observed in parallel when all three *ori*s were available (S12 Fig). This is indicative of a reduced number of replisome formations in SmABCΔoriV. Collectively, MFA and this microscopy data indicate that SmABCΔoriV contains a single 6.7 Mbp replicon.

188 **A triple color fluorescent labeling system for simultaneous microscopic monitoring of *oriC***
189 **and two further freely selectable genomic loci**

190 To enable live cell imaging analyses of spatial organization and spatiotemporal dynamics of the rearranged
191 genomic DNA in the replicon fusion strains SmAB, SmABC and SmABCΔoriV, we established a triple
192 color fluorescent labeling system. As this required using several antibiotic resistance markers, we
193 eliminated by homologous recombination the inactive *lox* sites together with the downstream resistance
194 markers that remained from the replicon fusion procedure in the AB and ABC DNA molecules (S1 and
195 S13A Fig). This gave rise to derivatives of SmAB, SmABC and SmABCΔoriV termed SmABΔR,
196 SmABCΔR and SmABCΔoriVΔR, respectively. The genome architecture of these strains was validated by
197 PFGE (S13B Fig) and Illumina genome sequencing.

198 ParB is known to specifically recognize and bind cognate *parS* sequences typically located around the
199 chromosomal origin of replication in various bacterial species [33]. This protein was previously reported to
200 be essential in *S. meliloti* [34] and used as marker for *oriC* in this bacterium [18,35]. Indeed, we found good
201 evidence for *C. crescentus*-like *parS* sites localized close to *oriC* in *S. meliloti* (S14C Fig). In our study, we
202 employed a ParB-cerulean fusion to label *oriC*. To this end, *parB* at its native chromosomal locus was
203 replaced by a *parB-cerulean* fusion in SmABΔR, SmABCΔR, SmABCΔoriVΔR, and the wild type
204 (S14A Fig). Growth of the parental strains and corresponding derivative strains was indistinguishable in
205 TY medium (S14B Fig), suggesting that the ParB-cerulean protein was functional.

206 In addition, a fluorescence repressor operator system (FROS) for labeling of two freely selectable
207 genomic loci was established. This system combined *tetO* and *lacO* operator arrays [36] with *tetR-mVenus*
208 and *lacI-mCherry* placed under control of the P_{tauA} promoter on the replicative and mobilizable low copy
209 vector pFROS (S14A Fig). In this setup, the basal activity of P_{tauA} [37] was sufficient to generate a well
210 detectable fluorescent signal over analysis periods of at least up to 6 hours in our study (S14D Fig), which
211 makes the system particularly suitable for time lapse applications.

212 **Polar or subpolar localization of the three replication origins at the old cell pole and polar**
213 **positioning of *terC* at the new cell pole was conserved in SmABC**

We asked for the effect of replicon fusions on the spatial organization of the genomic DNA in *S. meliloti* by comparing monopartite and tripartite genome architectures. To this end, SmABCΔR and wild type derivatives, both carrying the *parB-cerulean* marker, were equipped with *tetO* and *lacO* arrays for simultaneous labeling of *oriC*/*oriA*/*oriB*, *oriC*/*terC*, *oriC*/*oriA*/*terA* and *oriC*/ori*B*/*terB* (Fig 4A; S16A Fig). In addition, we constructed derivatives of both strains for simultaneous labeling of *oriC* via ParB-cerulean and one further genomic locus either by integration of a *tetO* or *lacO* array. The labeled positions included genomic loci adjacent to the sites used for fusion of the replicons (Fig 4A; S16A Fig). Prior to fluorescence microscopy analysis, these strains were validated by PFGE for their correct genome configuration (S15 and S18 Fig), and pFROS was introduced to mediate fluorescent labeling of the genomically integrated *tetO* and *lacO* arrays. For subcellular 2D mapping of the labeled genomic loci by snap-shot imaging of live cells, we filtered cells by size with a maximum cell length of 2.0 µm and displaying a single ParB-Cerulean-mediated fluorescent focus in one of the two cell pole regions only (Fig 4B). This configuration is indicative of a G_1-phase cell with *oriC* localized at the old cell pole [17,18]. On average, the cell lengths were 1.8 ± 0.1 µm for both wild type and SmABCΔR.

Plotting the subcellular location of individual markers as function of the genomic position showed a tripartite triangle pattern, indicating arrangement of DNA segments between *ori* and *ter* along the longitudinal cell axis (Fig 4C). In wild type and SmABCΔR, *oriC* and *oriA*/*oriB* occupied polar and subpolar areas, respectively (S16B Fig). As expected from our filtering approach and in agreement with previous reports [17, 18], in both strains, the *oriC* signal showed a very low positional variance at one cell pole (S1 Table). Subpolar localization of *oriA* and *oriB* signals with similar variances in both strains suggests a spatial confinement of these elements to this region of the cell (S1 Table).

The *terC* fluorescence signal was enriched with low positional variance at the cell pole opposite to the pole exhibiting the ParB-cerulean signal in wild type and SmABCΔR (S16B Fig; S1 Table). However, the average spatial positions of *terA* and *terB* signals differed between these strains (S16B Fig; S1 Table). Changes in spatial positions were also found for further markers. We particularly observed differences between the average positions of the fluorescent signals for markers 5/6, 9/10 and 15/16 flanking the

240 replicon fusions sites in SmABCΔR compared to the wild type (Fig 4C; S1 Table). This was expected since
241 the markers of each pair are situated on different DNA molecules in the wild type, whereas they were
242 brought into close proximity by the replicon fusions. In contrast, the average subcellular signal positions of
243 chromosomal markers 2, 3 and 18, which map in close vicinity to *oriC* or *terC*, did not much differ between
244 both strains (Fig 4D; S1 Table).

245 Tethering of *ori* and *ter* regions to factors localized at cell poles was previously reported for several
246 bacteria [38-42]. To test if the spatial organization of DNA in SmABCΔR is only determined by the
247 positioning of locally confined origin and terminus regions and the inherent features of the DNA as semi-
248 flexible polymer of compacted units, we simulated the DNA arrangement for genome configurations
249 differing in number and position of confined loci. We expanded a previously described model [43] by
250 implementing not only one origin and one terminus as possible fixpoints, but three of each. By ergodic
251 sampling over 200 configurations (Fig 4E) using the MOS-algorithm [44] the average genomic
252 organization was obtained.

253 Initially, we generated a model including only *oriC* (S17A Fig) and *oriC*/*terC* (S17B Fig) as anchoring
254 points of the 6.7 Mbp DNA molecule at the old and the new cell poles. We found that confining these two
255 loci are not sufficient to describe the spatial arrangement of pSymA- and pSymB-derived DNA. By
256 anchoring of all three origins to the experimentally determined average subcellular position, we gained a
257 ternary model structure with highly variable DNA segments between the three points (S17C Fig). However,
258 in this model structure, the DNA segment between *oriC* and *oriB* did not extend up to the opposite cell
259 pole. We then confined *terC* to the new cell pole, and *oriC* to the polar, and *oriA* and *oriB* to the subpolar
260 regions of the old cell pole (S17D Fig) since these loci showed the smallest positional variance in the
261 experimental data (S17E Fig). With these four anchored points the generated model structure already
262 reflected the experimentally determined positions of loci 2, 3 and 5 as well as locus 6 located on the
263 chromosome and pSymB, respectively. However, it did not describe the experimentally determined average
264 localization of *terA* and *terB*. Loci close to *terA* and *terB* showed a high positional variance in the

experimental data (S17E Fig). By a spatial confinement of *terA* and *terB* within the experimental data variance we gained a tripartite triangle structure (Fig 4F), albeit this model did not reproduce the experimentally determined average localization of loci 13 to 18.

Spatiotemporal dynamics of origin and terminus regions in replicon fusions strains

To study the effect of bi- and monopartite genome configurations and reduced number of replication initiation sites on DNA segregation, we analyzed the spatiotemporal dynamics of the replication origin and terminus regions in SmABΔR, SmABCΔR and SmABCΔoriVΔR in comparison to the wild type. For this purpose, we completed the set of strains carrying *tetO* and *lacO* arrays for labeling of replication origin and terminus regions. To this end, we integrated the corresponding constructs into the appropriate genomic positions of SmABΔR and SmABCΔoriVΔR, validated the genome configurations of the resulting strains by PFGE (S18 Fig), and introduced pFROS. At the level of individual cells, microscopic snap-shot and time lapse data of combinations of labeled *oriC*/*oriA*/*oriB*, *oriC*/*terC*, *oriC*/*oriA*/*terA* and *oriC*/*oriB*/*terB* were generated.

Spatiotemporal choreography of origins and termini was similar in the replicon fusion strains and wild type. Initially, the spatiotemporal dynamics of fluorescently labeled *ori* and *ter* loci in mother cells of *S. meliloti* wild type, SmABΔR and SmABCΔR were analyzed. For each individual cell analyzed, cell cycle duration and cell size were normalized to 100 % (0/100 % – completion of cell division) and to 1 (0 – old cell pole, 1 – new cell pole), respectively, to facilitate comparative analyses. In agreement with our previous study [18], in these three strains, two *oriC* foci, indicative of the start of chromosome segregation, were observed at the old cell pole (Fig 5B; S3 Table) shortly after completion of cell division (first quarter of the cell cycle, Fig 5A). This was followed by translocation of one of these *oriC* foci (*oriC2*) to the new cell pole (S19B, S21B and S23B Fig), and *oriC* segregation was mostly completed before cells reached the second quarter of the cell cycle (Fig 5Cii). In the three strains, *oriA* and *oriB* foci translocated from a subpolar region to the midcell area where duplication of both was observed after completion of *oriC* partitioning (Fig 5B). The visible segregation of these foci occurred in the second quarter of the cell cycle

(Fig 5A), on average 41.0 ± 12.4 min (*oriA*) and 48.2 ± 11.2 min (*oriB*) after *oriC* foci duplication (S29A Fig). Progression of this segregation resulted in localization of both an *oriA* and *oriB* copy in each subpolar region of the future sibling cells (S19A, S21A and S23A Fig).

Translocation of the *terC* foci from the new pole to midcell started in the three strains approximately in the middle of the cell cycle (Fig 5C). Two *terC* foci were observed at midcell for the first time in the last quarter of the cell cycle before cell division (Fig 5B and 5C). *terA* and *terB* foci already localized in the midcell area before duplicated foci were observed in this region (Fig 5B). Doubling of *terA* and *terB* foci was observed prior to *terC* segregation in the third quarter of the cell cycle (Fig 5A). In the daughter cells, choreography of individual *ori* and *ter* foci was similar to that in the mother cells described above (S27 and S28 Fig; S4 and S5 Table).

We asked if there is a preferential order of *oriA* and *oriB* segregation at the level of individual wild type, SmABΔR and SmABCΔR cells. Upon detailed examination, we found that duplication of *oriA* and *oriB* foci in both mother and daughter cells was very close in time (S19A, S21A and S23A Fig), and was observed either simultaneously (S29B Fig) or sequentially (Fig 5D), with *oriA* starting segregation before *oriB* in the majority of cells. In up to a fifth of wild type, SmABΔR and SmABCΔR cells analyzed (n=200 each), we found the doubling of *oriA* and *oriB* foci within the same time frame of 5 minutes (S29C Fig). In the remaining proportion of cells that showed sequential segregation of these origins, *oriA* segregation preceded that of *oriB* in three-fourth of these cells (Fig 5E). In conclusion, the time-lapse analyses of fusion strains SmABΔR and SmABCΔR indicate that choreography of origin and terminus regions, encompassing position and order of origin segregation events, resembles that of the wild type with a tripartite genome configuration.

Chronology of segregation and spatial position of *oriC* and Δ*oriA*/*B* regions are altered in SmABCΔoriVΔR. Strain SmABCΔoriVΔR carries monopartite genomic DNA containing *oriC* but lacking both secondary replicon origins (*repA1B1ΔC1,* Δ*oriB* and *repA2B2ΔC2,* Δ*oriA*). We studied the

314 segregation chronology of active *oriC*, inactive Δ*oriA/B*, and terminus regions in this strain to learn about
315 the segregation properties of the 6.7 Mbp single replicon.

316 In an initial fluorescence microcopy snapshot series, we analyzed putative G_1-phase SmABCΔoriVΔR
317 cells filtered with a cut-off of 2.0 µm cell length and deduced the relative distance of *oriC* and both Δ*oriA/B*
318 foci to the cell equator. Striking differences were found between *oriC* localization in SmABCΔoriVΔR
319 compared to wild type, SmABΔR and SmABCΔR cells. In SmABCΔoriVΔR cells, the distribution of *oriC*
320 localization showed two high-density clusters (S30 Fig), one in the cell pole (0.5 to 1 and -0.5 to -1) and
321 one in the midcell area (0 to 0.5 and 0 to -0.5), representing about 65 % and 35 % of the cells analyzed,
322 respectively (Fig 6A). In contrast, wild type, SmABΔR and SmABCΔR showed *oriC* foci clustering in the
323 cell pole area of 89 to 94 % of the cells analyzed (Fig 6A). We also observed that in SmABCΔoriVΔR,
324 both Δ*oriA/B* foci localized more frequently in the midcell area than in the cell pole area (S30 Fig) and
325 therefore analyzed the subcellular localization of these loci in correlation to *oriC* localization (S31 Fig).
326 Whereas only about 12 to 18 % of wild type, SmABΔR and SmABCΔR cells showed one or both Δ*oriA/B*
327 foci together with *oriC* in the midcell area, this was the case for 43 to 47 % of SmABCΔoriVΔR cells
328 (Fig 6B). Collectively, this data suggests aberrant localization of *oriC* in more than one third of
329 SmABCΔoriVΔR G_1 -phase cells.

330 To follow up on this observation, we performed time-lapse fluorescence microscopy. Analysis of this
331 data revealed two different *oriC* localization patterns in the two sibling cells (Fig 6C). In three fourth of
332 SmABCΔoriVΔR cells analyzed (n = 400), we found *oriC* localizing in one sibling in the midcell area
333 (sibling 1) and in the other sibling at the cell pole (sibling 2) right before cell division. We analyzed 20 of
334 the sibling 1 cells for the time point of visible *oriC* foci segregation and observed that this event occurred
335 in the first cell cycle quarter (Fig 5A). Following cell cycle progression of 80 sibling 1 cells revealed that
336 visible *oriC* foci segregation occurred in the midcell area (Fig 6D). In 81.3 % of these sibling 1 cells, right
337 before cell division, segregation of *oriC* foci resulted in localization of one *oriC* focus (*oriC2*) at the new
338 cell pole and the other (*oriC1*) in the mid-area of the mother cell compartment (S32 Fig). In the sibling 2

339 cells, we found duplication of the *oriC* focus (*oriC1*) at the old cell pole followed by translocation of one
340 of the *oriC* foci (*oriC2*) to the new pole (Fig 6D). Right before cell division, this resulted in *oriC2* foci
341 localized at the new cell pole in 86.3% of the cells and *oriC1* localized either at the old cell pole or in the
342 mid-area of the mother cell compartment in 30.0% and 70.0% of the cells, respectively (S32 Fig). We
343 identified the sibling 2 cells as the daughter cells since they most frequently adopted the *oriC* localization
344 pattern of the previous sibling 1 cell (i.e. mother cell) after one cell cycle. A schematic summary of the
345 predominant *oriC* segregation patterns in mother and daughter cells is shown in Fig 6E.

346 Moreover, we found that in mostly all mother cells analyzed displaying aberrant *oriC* localization the
347 Δ*oriA* and delta Δ*oriB* regions lost their subpolar localization (S25 and S26 Fig). This is in agreement with
348 our observation from the snapshot analysis. In addition to the change in the spatial position of the first
349 visible segregation of fluorescently labeled *oriC*, we also observed a change for Δ*oriB*. Whereas in wild
350 type, SmABΔR and SmABCΔR cells, duplication of labeled *oriB* occurred mostly at midcell, Δ*oriB*
351 duplication in SmABCΔoriVΔR cells was observed in the new cell pole compartment (Fig 5B).

352 In SmABCΔoriVΔR, wild type, SmABΔR and SmABCΔR mother cells, we observed two different
353 temporal patterns of fluorescent foci duplication associated to *ori* and *ter* regions. Cells of the latter three
354 strains showed arrival of the *oriC2* focus at the new cell pole approximately in the end of the first cell cycle
355 quarter and *terC* focus translocation from the new cell pole to the midcell area shortly after the midpoint of
356 the cell cycle. In SmABCΔoriVΔR cells, however, *terC* focus translocation occurred already in the
357 beginning of the second cell cycle quarter, whereas no clear difference was observed for the timepoint of
358 *oriC2* focus arrival at the new cell pole (Fig 5Cii). In these cells, doubling of *terC* and also of *terA* foci was
359 predominantly observed in the second cell cycle quarter, whereas these events occurred in the last and third
360 cell cycle quarter, respectively, in the three other strains (Fig 5A). Moreover, two foci representing the
361 *ΔoriA* regions were observed for the first time in SmABCΔoriVΔR cells shortly after the halfway point of
362 the cell cycle, in contrast to duplication of the corresponding regions in cells of the other strains in the
363 second quarter of the cell cycle (Fig 5A). Thus, in SmABCΔoriVΔR cells, visible segregation of *terA*

364 occurred before that of the Δ*oriA* region. Duplication of *terB* and Δ*oriB* foci was observed mostly at the
365 end of the third cell cycle quarter, with duplication of *terB* in SmABCΔoriVΔR cells occurring on average
366 before that of Δ*oriB* (Fig.5A). In wild type, SmABΔR and SmABCΔR cells, duplication of *oriB* was
367 observed already in the second cell cycle quarter followed by *terB* duplication in the third cell cycle quarter.
368 Similar differences in chronology of foci duplication were also observed when daughter cells of
369 SmABCΔoriVΔR were compared with wild type, SmABΔR and SmABCΔR (S27 Fig; S4 Table).

370 **A missense mutation in cell cycle kinase-encoding *cckA* is not responsible for aberrant *ori***
371 **localizations in SmABCΔoriVΔR but probably increased fitness of this strain**

372 In addition to genome sequencing of SmAB, SmABC, and SmABCΔoriV (see above), we also determined
373 the genome sequence of SmABΔR, SmABCΔR, and SmABCΔoriVΔR (S8 Table). In particular, a SNV in
374 the coding sequence *SMc00471* of the cell cycle histidine kinase CckA in SmABCΔoriVΔR attracted our
375 attention. This SNV that causes amino acid substitution R436H (S33A Fig; S8 Table) was not found in the
376 precursor strains.

377 To test whether this missense mutation was responsible for the aberrant *oriC* localization pattern in
378 strain SmABCΔoriVΔR we attempted to revert the SNV to the wild-type *cckA* sequence in this strain, and
379 failed. We then introduced this missense mutation into the wild type and SmABCΔR and analyzed the
380 localization of *oriC* right before cell division in G_1-phase cells, using ParB-Cerlulean for fluorescent
381 labeling (Fig 7A; S33B and S33C Fig). Regarding polar (approx. 90 %) and midcell (approx. 10 %)
382 localization of the ParB-Cerlulean mediated fluorescent focus, we found no difference between the strains
383 carrying the SNV in *cckA* and the corresponding strains with wild type *cckA* (Fig 7A). However, in this
384 comparison, growth of the strains with $CckA^{R436H}$ was slightly reduced (S33D Fig).

385 In addition, we used ParB-Cerlulean to analyze the *oriC* localization pattern in SmABCΔoriV, the direct
386 precursor of SmABCΔoriVΔR. SmABCΔoriV carries the *cckA* wild type sequence and is already deleted
387 for both secondary replicon replication origins (Δ*oriA*/*B*). We found that the *oriC* localization pattern in
388 SmABCΔoriV already deviates from the wild type-like pattern in SmABC, which has three intact

389 replication origins (Fig 7B). This implies that CckA^{R436H} did not cause the observed mislocalization of *oriC*
390 in SmABCΔoriVΔR. However, we found a strong difference in growth between SmABCΔoriV (CckA) and
391 SmABCΔoriVΔR (CckA^{R436H}) (S33E Fig.), indicating that the *cckA*$_{R436H}$ allele mitigates growth
392 deficiencies of SmABCΔoriVΔR.

393 ## ■ DISCUSSION

394 Although the universal single DNA replication origin paradigm for genomic DNA molecules seems to be
395 true for most bacterial species, natural strain isolates containing chromosomes derived from cointegration
396 of two or three replicons were found [7-10]. Previous studies of engineered *E. coli* strains indicate that
397 disturbing chromosome organization patterns by integration of one or more additional *oriC* copies or re-
398 localization of *oriC* to ectopic locations can cause replication-transcription conflicts and issues with
399 replication fork trap regions, which affect DNA replication and segregation, and promote selection of
400 phenotype-moderating genome rearrangements and genetic suppressions [11,12,45-48]. In naturally
401 occurring single-chromosome Vibrio (NSCV) strains of *V. cholerae*, a second origin was found to be either
402 active or silenced depending on the position of the cointegration event [49], whereas in laboratory-generated
403 fusions the Chr2 replication machinery was not functional [50,51]. These findings motivated us to ask about
404 the effects of multiple replication origins and terminus regions in cointegrated bacterial replicons on spatial
405 DNA organization and spatiotemporal patterns of replicon segregation.

406 We addressed these questions by converting the *S. meliloti* tripartite genome configuration into bi- and
407 monopartite configurations. This set-up differed in several features from the engineered *E. coli* strains with
408 multiple copies of *oriC* in the main chromosome. The *S. meliloti* replicon fusion strains have three different
409 distinct origins of replication, each associated with a replicon-specific partitioning system [23]. Differential
410 regulation of the activities of these origins promotes sequential replication initiation in the wild type during
411 the cell cycle [18]. In the fused replicons, we aimed at retaining organizational properties of the replicons,
412 such as GC skew, and distribution and orientation of KOPS and coding sequences. This was also the case
413 for a natural occurring *S. meliloti* triple replicon cointegrate [7], which we approximately reproduced. Our

414 replicon fusion strategy by site-specific recombination reduced the likelihood of homologous
415 recombination-mediated revertants, reported for the natural occurring *S. meliloti* triple replicon cointegrate
416 [7]. This enabled investigating spatial DNA organization and spatiotemporal segregation patterns of a
417 monopartite triple-replicon bacterial genome, mostly independent of aberrant replicon symmetry patterns
418 and spontaneously occurring genome rearrangements in the studied strains.

419 **Spatial organization and spatiotemporal segregation patterns of the engineered monopartite**
420 **triple-replicon genome.** We found that DNA replication initiated at all three origins in the triple replicon
421 fusion strain. Conservation of replichore asymmetries in the *oriC*-*oriB* and *oriB*-*oriA* segments, and
422 termination regions close to or overlapping the termination regions of the wild type argue for retained
423 differences in the progression of the replication forks, e.g. by replication fork trapping sequences that slow
424 down or stall the replisome [52]. This is contrary to what has been observed with *V. cholerae* [53]. The
425 conservation of *terC* in the single replicon strain SmABCΔoriVΔR, with even extremely skewed
426 replichores, provides clear evidence for mechanisms defining this region for termination in the replication
427 process and for spatial organization.

428 Compared to the wild type, the engineered strain was unremarkable in morphology and growth behavior
429 in complex medium, indicating that the new genome configuration does not significantly interfere with cell
430 proliferation processes. However, high-salinity and hyperosmotic stress weakly reduced growth. High salt
431 conditions are known to influence the supercoiling state of genomic DNA [54], thus, the triple replicon
432 fusion strain may be somewhat less robust to conditions affecting DNA condensation.

433 In many bacteria, tethering of the chromosomal origin and terminus regions to cell poles plays an
434 important role for spatial chromosome organization and segregation [55]. Previously, a longitudinal *oriC*
435 (old pole)-*terC* (new pole) configuration of the main chromosome and subpolar localization (old pole) of
436 the *ori*s of the secondary replicons was reported for *S. meliloti* G_1-phase cells with tripartite genome
437 configuration [17,18]. Combining fluorescence microscopy and DNA random walk modeling, we found
438 that polar localization of *oriC* and *terC* as well as subpolar localization of *oriA* and *oriB* are maintained in

439 cells of the *S. meliloti* triple replicon fusion strain, and thus significantly contribute to spatial organization
440 of the genomic DNA.

441 In many bacterial species with polarly localized *oriC*, the DNA-binding CTPase ParB [56, 57] binds to
442 clusters of *parS* sequences in the *ori* region. It tethers this DNA region to a cell pole-associated protein
443 scaffold once sister *ori* segregation is finished, acting as a landmark for the following segregation of the
444 bulk of chromosomal DNA [56]. At both poles of *C. crescentus* cells, PopZ forms a scaffold interacting
445 with ParB-*parS* [39,40]. In *Agrobacterium tumefaciens* (*Rhizobium radiobacter*), which like *S. meliloti*
446 belongs to the *Rhizobiaceae*, the PopZ ortholog was observed at the new pole shortly after cell division
447 [58]. This makes it unlikely that PopZ is involved in the spatial confinement of *oriC* in the old cell pole
448 region in this species. Similar to its functional role in *C. crescentus*, PopZ may play a role in binding one
449 *oriC* copy to the new cell pole in the process of chromosome partitioning [39,40]. In *A. tumefaciens*, the
450 polar organelle development (Pod) protein PodJ localizes at the old pole [59] and is essential for tethering
451 the *ori*s of its main circular and its secondary linear chromosome to this pole in early phases of the cell
452 cycle [60]. However, in *S. meliloti*, the ortholog PodJ1, which is a truncated version of PodJ, was only
453 detected at the new cell pole [61], making its involvement in anchoring *oriC* to the old pole unlikely.
454 Therefore, the pole organizing factor(s) tethering *oriC* to the old cell pole remain(s) to be identified in *S.*
455 *meliloti*.

456 Factors that mediate spatial confinement of *oriA* and *oriB* to subpolar regions in *S. meliloti* are also still
457 unknown. In *Myxococcus xanthus*, bactofilins that assemble into elongated scaffolds restrain the ParAB*S*
458 chromosome segregation machinery and thereby the chromosomal origin of replication to the subpolar
459 region [62]. It is conceivable that similar cytoskeletal filaments mediate spatial confinement of *oriA* and
460 *oriB* to the subpolar region in *S. meliloti*. This might also explain the greater cell-to-cell variance in spatial
461 positions of these *ori*s in the subpolar region compared to the spatially less variable polar localization of
462 *oriC*.

463 Localization of *terC* at the old cell pole of G_1-phase cells showed a very low cell-to-cell variance of
464 spatial positions in the triple replicon fusion strain, which is likely mediated by orthologs of factors known

to be involved binding *terC* at the old cell pole in *C. crescentus* (see discussion below) [63, 64]. In contrast, cell-to-cell variance of the spatial positions of the terminus regions of the secondary replicons was high. Nevertheless, constraints on the diffusion of *terA* and *terB* within the limits of the observed variance were necessary for our *in silico* simulations to approximately reproduce the experimental observations. The spatial shift of *terA* in the triple replicon fusion strain argues against active positioning. We therefore speculate that these regions are subject to constraints on mobility, possibly due to a gradient of potential binding sites or inherent properties of the cytoplasm, such as molecular crowding [65,66] and viscosity influencing size-dependent motions of molecules [67].

The almost complete correspondence of the spatiotemporal segregation pattern of the origin and terminus regions of the three replicons in the wild type and in the triple replicon fusion strain indicates that the regulation of replication initiation and the processes relevant to segregation have been conserved. Consistent with a previous study [18], duplication and segregation of *oriC* commenced before these processes started for the *ori*s of the secondary replicons, with a strong preference for *oriA* preceding *oriB*. However, in the current study, which examined a much larger number of cells compared with the previous study [18], the previously observed temporal order of duplication and segregation first of *oriA* and then of *oriB* was less stringent. The mechanism of coordination of replication initiation of secondary replicons with that of the chromosome in *S. meliloti* is still unknown. Transcriptome data [68] and DNA methylation pattern [69] of a *S. meliloti* wild type strain also suggest an asynchronous replication of the chromosome and the secondary replicons. Stronger upregulation of *repC2* (pSymA) than *repC1* (pSymB) transcripts during the cell cycle [68] might indicate a threshold-like mechanism contributing to the temporal preference for *oriA* replication initiation. In *C. crescentus*, the interplay of CcrM with GcrA is suggested to mediate methylation state dependent regulation of gene expression [70,71]. Since in *S. meliloti,* these two cell cycle regulators are conserved [70,72] and recognition motifs of the N6-adenosine methyltransferase CcrM were found upstream of cell cycle-regulated genes of the *repABC* loci on the secondary replicons [69], methylation state dependent regulation of gene expression is hypothesized to also contribute to the integration of these replicons in the cell cycle.

We propose that translocation of *terC* from the new cell pole to midcell, observed approximately midway of the cell cycle in the *S. meliloti* wild type and triple fusion strain, is controlled by a mechanism similar to that suggested for *C. crescentus*. For most of the cell cycle, the replication terminus of the *C. crescentus* chromosome is colocalizing with FtsZ, which accumulates at the new cell pole in G_1-phase cells and forms the Z-ring in the midcell region towards the end of the cell cycle [63]. Spatial coupling of both is mediated by interaction of the terminus recognition protein ZapT [63], the Z-ring associated proteins ZapA [73] and ZauP [64,74]. A potential homolog of ZapA (SMc03976) was reported in *S. meliloti* [75] and we found a candidate for a ZapT homologue (SMc01787) by sequence comparisons.

Spatial organization and spatiotemporal segregation patterns of the engineered monopartite single-replicon genome. Replicon fusions made initiator protein-encoding *repC* genes including the replication origins of the secondary replicons dispensable. This suggests that replisomes that initiated replication at *oriC* were not ultimately stalled in the original pSymA- and pSymB-derived terminus regions. Nevertheless, sequential deletion of secondary replicon-derived *ori*s in strains with bi- or monopartite genome configuration was associated with reduced growth, possibly due to replication obstacles arising from the new replichore structures.

Consistent with *oriC* and *terC* providing the main landmarks for DNA replication and segregation processes in the monopartite single-replicon strain, chronology of segregation of Δ*oriA/B* and *ter* loci changed compared to the monopartite triple-replicon strain. Segregation of these loci correlated with the position on the replicon sequence and the distance to *oriC*. Remarkably, we found that *oriC* and both Δ*oriA/B* loci lost polar and subpolar localization, respectively, in mother cells of the monopartite single-replicon strain. This suggests that the *repC* and *oriV* deletions directly or indirectly affect mechanisms relevant for anchoring of these sequence elements.

Based on our data, we hypothesize that the R436H amino acid substitution in CckA is a suppressor mutation that attenuates the growth deficiencies of the *S. meliloti* strain with monopartite single-replicon genome configuration constructed in this study. Cell cycle regulation by the CckA-ChpT-CtrA signaling pathway is wide-spread in α-proteobacteria [76]. The CckA phosphorelay controls the phosphorylation

status of ChpT which in turn regulates activity and stability of the cell cycle master regulator CtrA through phosphorylation [77]. CckA phosphatase activity enables initiation of DNA replication through dephosphorylation and degradation of CtrA [77,78]. The *S. meliloti* (S33A Fig) and *C. crescentus* CckA domain composition [79] is very similar. The R436H substitution in *S. meliloti* CckA locates in one of the PAS domains, which in *C. crescentus* were shown to regulate switching between the CckA kinase and phosphatase activities [79,80]. Narayanan and coworkers [81] identified a point mutation in the PAS-B domain of *C. crescentus* CckA that suppresses a topoisomerase IV inhibitor-induced chromosome segregation defect, possibly by slowing down the chromosome replication cycle. $CckA^{R436H}$ is therefore proposed to mitigate chromosome replication and/or segregation defects in a similar manner. We speculate that the R436H substitution promotes kinase or reduces phosphatase activity of *S. meliloti* CckA, which results in higher levels of CtrA-P repressing replication initiation and slowing down the cell cycle.

■ MATERIALS AND METHODS

Bacterial strains and cultivation conditions. Bacterial strains used in this study are derivatives of *E. coli* K12 and *S. meliloti* Rm1021 (S9 Table). *E. coli* was grown at 37°C in lysogeny broth (LB) medium [82, 83]. *S. meliloti* strains were cultivated at 30°C in either tryptone yeast extract (TY) medium [84] or modified morpholinepropanesulfonic acid (MOPS)-buffered minimal medium [85] at 200 rpm. If required, the following antibiotics were used accordingly: gentamicin (8 µg/ml for *E. coli*, 30 µg/ml for *S. meliloti*), kanamycin (50 µg/ml for *E. coli*, 200 µg/ml for *S. meliloti*), streptomycin (600 µg/ml for *S. meliloti*), spectinomycin (100 µg/ml for *E. coli*, 200 µg/ml for *S. meliloti*) or tetracycline (10 µg/ml for *E. coli* and 3 µg/ml for *S. meliloti*). Solid medium was supplemented with 1.5% (w/v) BD Difco™ technical agar (Fisher Scientific).

DNA manipulation and plasmid extraction. Plasmids used in this study are listed in S10 Table. Standard molecular techniques were employed for cloning and transfer of nucleic acids [83]. DNA fragments were PCR amplified using Q5® High-Fidelity DNA Polymerase (New England Biolabs) or Taq DNA Polymerase (New England Biolabs). DNA oligonucleotides were provided by Sigma-Aldrich (USA) and

Integrated DNA Technologies (USA) (S13 Table). For DNA purification and gel extractions the E.Z.N.A.® Cycle-Pure Kit (Omega Bio-Tek) and illustra™ GFX™ PCR DNA and Gel Band Purification Kit (GE Healthcare Life Sciences) were used, respectively. For phosphorylation of the 5′ hydroxyl terminus of PCR amplicons and oligonucleotides T4 Polynucleotide Kinase (Thermo Scientific) was applied. Dephosphorylation of DNA ends was performed by use of FastAP™ Thermosensitive Alkaline Phosphatase (Thermo Scientific). The fill in of 5′-overhangs in double stranded DNA to form blunt ends was achieved using the large fragment of DNA Polymerase I (Klenow fragment) (Thermo Scientific). T4 Ligase (Thermo Scientific) was used for ligation. Plasmid DNA was isolated using the "E.Z.N.A. Plasmid Mini Kit" (Omega Bio-Tek). All enzymatic catalyzation and purification steps were performed according to the manufacturer's protocols and instructions. For sequence verification of plasmid and amplified DNA the sanger sequencing service of Eurofins Genomics (Germany) was used. For detailed information on the construction of individual plasmids refer to S12 Table.

Strain construction. Strains generated in this study are listed in S11 Table. Transfer of plasmids to *S. meliloti* was achieved by conjugation using *E. coli* S17-1 [86] or by electroporation as previously described [25]. Cells for electroporation were prepared as described in Ferri et al. [87]. Markerless integrations through double homologous recombination were carried out using pK18mobsacB derivatives and sucrose selection [88].

On the basis of a Cre/*lox* toolbox and *S. meliloti* Rm1021 derivative SmCreΔhsdR [25] the tripartite genome was merged in two consecutive steps. First, pSymA and pSymB were fused with each other, giving rise to the megaplasmid hybrid pSymAB harbored by *S. meliloti* strain SmAB. Therefore, pK18mobsacB derivatives pJD98 and pJD99 were used to integrate *lox* sites and antibiotic selection markers into SmCreΔhsdR for the site-specific recombination. After removal of active *lox* sites, SmAB was sequentially transformed with constructs pJD130 and pJD126 again providing *lox* sites and an additional antibiotic selection marker for integration of the chromosome and pSymB. Cre-mediated integration of pSymAB into the chromosome gave rise to SmABC with monopartite genome configuration. Cre/*lox* applications were

performed as described before [25]. Illustration of SmAB and SmABC strain generation and detailed information about the construction process is given in S1 Fig and S11 Table, respectively.

In order to remove DNA replication origins of strain SmABC, deletion constructs pJD201 and pJD202 were used for sequential excision of the megaplasmid-encoded copies of *repC* and corresponding *repBC* intergenic regions. The deletion of both regions in SmABC resulted in strain SmABCΔoriV. By use of deletion constructs pJD222 and pJD229, *S. meliloti* strains SmAB, SmABC and SmABCΔoriV were further cured from spectinomycin and gentamicin resistance cassettes, respectively, giving rise to strains SmABΔR, SmABCΔR and SmABCΔoriVΔR accessible for constructs of the replicon labeling system. For *in vivo* studies of DNA organization and spatiotemporal dynamics of origin and terminus by fluorescence microscopy, a triple label system based on the fluorescent reporter gene fusions *tetR-mVenus* and *lacI-mCherry* (derived from the FROS [36]) and *parB-cerulean* was developed. Initially, *S. meliloti* strains SmCreΔhsdR, SmABΔR, SmABCΔR and SmABCΔoriVΔR were transformed with pMW198. Deletion of the plasmid backbone via sucrose selection resulted in an in-frame fusion of the native *parB* gene with *cerulean* (*oriC* label). For analysis of the replisome formation and dynamics pK19ms DnaN-mCherry [18] was used for markerless integration of the fluorophore. pK18mobsacB derivatives pMW186 (providing 120 copies of the *tetO* array, $tetO_{120}$) and pMW188 (carrying 120 copies of the *lacO* array, $lacO_{120}$) were used for marker-free labeling of *oriA* (SMa2383 - SMa2385 intergenic region) and *oriB* (SMb20041 - SMb20042 intergenic region), respectively. pK18mob2 derivatives pJD169 ($tetO_{120}$), pMW193 ($lacO_{120}$) and pJD170 ($tetO_{120}$) enabled labeling of *terC* (SMc01205 - SMc01204 intergenic region), *terA* (SMa1188 (*nosX*) - SMa1191 (*hmp*) intergenic region) and *terB* (SMb21555 (*kefB2*) - SMb21556 intergenic region), respectively. Regarding the *ori/ter* labeling, *oriC* pre-labeled strains were transformed with pJD169 (*oriC*/*terC* labelling), pMW186 and pMW193 (*oriC*/*oriA*/*terA* labelling), or pMW188 and pJD170 (*oriC*/*oriB*/*terB* labelling). Additionally, integrative pK18mob2 derivatives pAM25, pAM30, pAM31, pAM32 (Km^R, $tet0_{120}$) and pACYC177 derivatives pAM7, pAM13, pAM45, pAM47, pAM68, pAM69, pAM70 and pAM72 (Gm^R, $lacO_{120}$) were used to label further genomic loci in context of the genome organization analysis. Repair of $CckA^{R436H}$ in SmABCΔoriVΔR was attempted using a double homologous

593 recombination strategy integrating pMW257 for markerless replacement of the *cckA* SNV (C→T) with wild
594 type coding sequence of *cckA*. Reproduction of the CckA^{R436H} mutation in strains of the wild type and
595 SmABCΔR was achieved by markerless integration of *cckA* SNV (C → T) trough pMW256. Analysis of
596 *oriC* localization in strains SmABC and SmABCΔoriV was realized by single crossover integration of
597 pMW261.
598 **Strain validation.** Pulsed-Field Gel Electrophoresis (PFGE) was used as method to validate the genome
599 architecture after major fusion and integration/deletion steps. The applied PFGE protocol for DNA
600 preparation and digestion was carried out as described for strain validations in Checcucci et al. [89]. To
601 gain fusion strain characteristic banding patterns the restriction digestion of genomic DNA was performed
602 with PacI (New England Biolabs, USA). For PFGE analysis, ¼ agarose plug with treated genomic DNA
603 was separated in an 0.7% agarose gel (Pulse Field Certified Agarose, Bio-Rad, USA) and 0.5x TBE buffer
604 at 12°C (44.5mM Tris-HCl, 44.5mM boric acid, 1mM EDTA) using the Rotaphor® System 6.0 (Analytik
605 Jena, Germany) according to the manufacturer's instructions. Separation of DNA fragments was achieved
606 with 130V-100V for 50-175sec at 130°-110° (run time 18h), 130V-80V for 175sec-500sec at 110° (run
607 time 18h) and 80V-50V for 500sec-2000sec at 106° (run time 40h) with a logarithmic course of increase or
608 decrease between varying parameters, respectively.
609 For sequence specific analysis, including verification of proper deletions and detection of single-nucleotide
610 variants (SNVs), all basic strains (SmCreΔhsdR, SmAB, SmABC, SmABCΔoriV, SmABΔ, SmABCΔR
611 and SmABCΔoriVΔR) were subjected to next generation DNA sequencing using the MiSeq™ System
612 (Illumina, USA). For preparation of genomic DNA, *S. meliloti* cells were grown in TY supplemented with
613 appropriate antibiotics and harvested at optical density$_{600}$ (OD_{600}) of 1.0 by centrifugation at 3000g (4°C).
614 Sample preparation was performed as previously described [90]. The investigation for single nucleotide
615 variations was carried out using the Basic Variant Detection tool (v.2.1) of CLC genomic workbench
616 (v.20.0.4) with a minimum coverage of eight, minimum count of four and minimum frequency of 50% for
617 mapped reads. In a next step each SNV was analysed manually by eye and additionally validated by sanger
618 sequencing in case of questionables.

Growth experiments. Prior to inoculation, overnight cultures were washed with 0.9% NaCl and adjusted to OD_{600} of 0.01-0.15 in TY or MOPS buffered medium supplemented with 600mg/ml streptomycin. Incubation Cultures were incubated in a 100 µl volume in a 96 well microtiter plate at 30°C and with shaking at 200 rpm. OD_{600} of cell cultures was measured every 30 min with a microplate reader (Tecan Infinite 200 PRO, Tecan, Switzerland).

Live cell microscopy and image analysis. *S. meliloti* cell cultures were grown in TY medium (glass tubes) supplemented with suitable antibiotics to OD_{600} of 0.25 for time lapse and OD_{600} of 0.5 for snapshot microscopy. To enrich cultures with G_1-phase cells for snapshot analysis, strains were grown to OD_{600} of 1.6 - 1.8, diluted to OD_{600} of 0.5 and subsequently used for microscopy. 1 µl of these cultures were then placed onto 1 % (w/v) molecular biology-grade agarose (Eurogentec, Belgium) pads containing ddH_2O (snap shots) or MOPS minimal medium and suitable antibiotics (time lapse), covered with a cover glass and sealed with VALAP [91]. For visual examination of *S. meliloti* cells by phase contrast and epifluorescence microscopy an Eclipse Ti-E inverse research microscope (Nikon, Japan) equipped with a 100x CFI Plan Apo1 oil objective (numerical aperture of 1.45), a green DPSS solid state laser (561 nm, 50 mW; Sapphire) and a multiline Argonlaser (457/488/514 nm, 65 mW; Melles Griot) with AHF HC filter sets F36-513 DAPI (excitation band pass [ex bp] 387/11 nm, beam splitter [bs] 409 nm, emission [em] bp 447/60 nm), F36-504 mCherry (ex bp 562/40 nm, bs 593 nm, em 624/40 nm), F36-528 mVenus (ex bp 500/24 nm, bs 520 nm, and em bp 542/27 nm) was used. Exposure times ranged from 200 ms to 2 s. Image acquisition and adjustment was done with an Andor iXon3 885 electron-multiplyingcharge-coupled device (EMCCD) camera and the software NIS-Elements v.4.13 (Nikon, Japan), respectively. Time-lapse analysis was performed at 30°C in a microscope incubator and images were acquired every 2 or 5 minutes. Analysis of snap-shot and time-lapse microscopy images was performed using ImageJ plug-in MicrobeJ [92]. G_1-phase cells were filtered for a maximal length of 2.0 µm and presence a single ParB-cerulean focus indicative of non-segregated *oriC*.

Marker frequency analysis. For marker frequency analysis, *S. meliloti* strains SmABC and SmABCΔoriV were grown in 50 ml TY medium supplemented with 600 mg/ml streptomycin at an initial OD_{600} of 0.1.

After incubation at 30°C and 200 rpm, samples were taken at OD_{600} of 0.6 (exponential phase) or OD_{600} of ~ 2.6 (overnight culture, stationary phase). Cells were harvested by centrifugation (4000 g, 4°C) and immediately frozen in liquid nitrogen. Preparation and acquisition of Illumina Miseq data were performed as previously described [90]. Paired-end reads were then mapped by the QuasR R package (v1.6.2) onto the *S. meliloti* replicons. Only unique hits were considered. Subsequently, the coverage was determined from the obtained mapped genomic DNA reads using the genomecov from the bedtools toolbox (v2.25.0). The average coverage of all samples ranged between 18 and 23. The coverage was normalized by the total coverage (sum of coverage) of each sample. To identify minimal variations in the copy number along the replicons, we used sliding window averaging. The size of the window comprised 200 kb. After averaging, the value at a certain position reflects the average coverage of about 2 % of the replicon left and right of the indicated position. This process averages out random noise and local sequence specific variation. To determine the copy number without prior information about the terminus region, the lower 10 % quantile of all windows was used to determine the reads in the terminus region. All windows where then normalized by this value, resulting in a copy number relative to the terminus region.

Modeling. For the simulations we used a model for DNA described by Buenemann and Lenz [43]. The basic assumptions of the model are 1) DNA can be modeled as a sequence of compacted units (S1 Text); 2) compact units can be restricted in their spatial arrangement e.g. by the action of proteins; and 3) The measured organization of the chromosome in the cell results from averaging over many individual configurations that meet these constraints. For *C. crescentus* this model revealed that self-avoidance of DNA, specific positioning of the origin (and terminus) region and the compaction of DNA are sufficient to explain the strong linear correlation between specific positions on the chromosome and their longitudinal arrangement within the cell [43]. To predict the spatial organization of the merged replicons in the *S. meliloti* replicon fusion strain SmABC an expansion of the model by implementing not only one origin and one terminus as fixpoints, but three each was done. For realization, the A* algorithm was added to the model, which made it possible to generate random walks between any number of fixed points (S2 Text).

Bioinformatic analysis. GC and GC^c skew analysis of the tri-, bi- and monopartite *S. meliloti* genome was performed using GenSkew (http://genskew.csb.univie.ac.at, Feb. 2020). GC skew depictions of the individual replicons as shown in Fig 1 were generated using the CGView server (http://stothard.afns.ualberta.ca/cgview_server/ Feb. 2020). Oligonucleotide skews for KOPS were calculated with fuzznuc (http://emboss.toulouse.inra.fr/cgi-bin/emboss/fuzznuc?_pref_hide_optional=1, Mar. 2020). Functional domain analysis of *S. meliloti* CckA was done using the NCBI conserved domain database (CDSEARCH/cdd) [93-95] with low complexity filter**,** composition-based adjustment and an E-value threshold of 0.01 (Oct. 2021).

Data Availability Statement.

The sequence data presentet in this article are available at the ArrayExpress Archive under the accession number (*to be provided*).

■ ACKNOWLEDGMENTS

Whole genome sequencing was performed by the Screening and Automation Technology Core Facility (SAT) of the Center for Synthetic Microbiology (SYNMIKRO). We thank Bernadette Boomers for technical assistance, Elizaveta Krol for providing primers, plasmids pG18mob-mVenus and pSRKGm-CmChr as well as for identification of a *S. meliloti* ZapT homologue, Anna Motnenko for providing pAM labeling plasmids, Yannick End for plasmid pYEM1, Vanessa Munoz-Gutierrez for providing primers and Patrick Manz for technical support related to microscopy. This study was supported by the Collaborative Research Centre TRR 174 “Spatiotemporal dynamics of bacterial cells” (German Research Foundation) and the LOEWE program of the State of Hesse (Germany).

■ AUTHOR CONTRIBUTIONS

AB, MW and JD designed the experiments. MW and JD carried out the experiments and analyzed the experimental data. PS performed computational analysis of sequence data for MFA. MW and JS analyzed genome sequence data. DG and PL modeled the spatial organization of DNA. AB and MW wrote the paper.

■ ABBREVIATIONS

ori - origin

ter - terminus

SNV - single nucleotide variation

MFA - marker frequency analysis

■ REFERENCES

1. Harrison PW, Lower RP, Kim NK, Young JP. Introducing the bacterial 'chromid': not a chromosome, not a plasmid. *Trends Microbiol*. 2010 Apr;18(4):141-8. doi: 10.1016/j.tim.2009.12.010.

2. diCenzo GC, Finan TM. The divided bacterial genome: structure, function, and fvolution. *Microbiol Mol Biol Rev*. 2017 Aug 9;81(3):e00019-17. doi: 10.1128/MMBR.00019-17.

3. Leonard AC, Méchali M. DNA replication origins. *Cold Spring Harb Perspect Biol*. 2013 Oct 1;5(10):a010116. doi: 10.1101/cshperspect.a010116.

4. Dewar JM, Walter JC. Mechanisms of DNA replication termination. *Nat Rev Mol Cell Biol*. 2017 Aug;18(8):507-516. doi: 10.1038/nrm.2017.42.

5. Ekundayo B, Bleichert F. Origins of DNA replication. *PLoS Genet*. 2019 Sep 12;15(9):e1008320. doi: 10.1371/journal.pgen.1008320.

6. Xia X. DNA replication and strand asymmetry in prokaryotic and mitochondrial genomes. *Curr Genomics*. 2012 Mar;13(1):16-27. doi: 10.2174/138920212799034776.

7. Guo X, Flores M, Mavingui P, Fuentes SI, Hernández G, Dávila G, et al. Natural genomic design in *Sinorhizobium meliloti*: novel genomic architectures. *Genome Res*. 2003 Aug;13(8):1810-7. doi: 10.1101/gr.1260903.

8. Chapman C, Henry M, Bishop-Lilly KA, Awosika J, Briska A, Ptashkin RN, et al. Scanning the landscape of genome architecture of non-O1 and non-O139 *Vibrio cholerae* by whole genome mapping reveals extensive population genetic diversity. *PLoS One*. 2015 Mar 20;10(3):e0120311. doi: 10.1371/journal.pone.0120311.

9. Xie G, Johnson SL, Davenport KW, Rajavel M, Waldminghaus T, Detter JC, et al. Exception to the rule: genomic characterization of naturally occurring unusual *Vibrio cholerae* strains with a single chromosome. *Int J Genomics*. 2017;2017:8724304. doi: 10.1155/2017/8724304.

10. Yamamoto S, Lee KI, Morita M, Arakawa E, Izumiya H, Ohnishi M. Single circular chromosome identified from the genome sequence of the *Vibrio cholerae* O1 bv. El Tor Ogawa strain V060002. *Genome Announc*. 2018 Jun 21;6(25):e00564-18. doi: 10.1128/genomeA.00564-18.

11. Wang X, Lesterlin C, Reyes-Lamothe R, Ball G, Sherratt DJ. Replication and segregation of an *Escherichia coli* chromosome with two replication origins. *Proc Natl Acad Sci U S A*. 2011 Jun 28;108(26):E243-50. doi: 10.1073/pnas.1100874108.

12. Dimude JU, Stein M, Andrzejewska EE, Khalifa MS, Gajdosova A, Retkute R, et al. Origins left, right, and centre: increasing the number of initiation sites in the *Escherichia coli* chromosome. *Genes* (Basel). 2018 Jul 27;9(8):376. doi: 10.3390/genes9080376.

13. Wang X, Montero Llopis P, Rudner DZ. Organization and segregation of bacterial chromosomes. *Nat Rev Genet*. 2013 Mar;14(3):191-203. doi: 10.1038/nrg3375.

14. Nielsen HJ, Ottesen JR, Youngren B, Austin SJ, Hansen FG. The *Escherichia coli* chromosome is organized with the left and right chromosome arms in separate cell halves. *Mol Microbiol*. 2006 Oct;62(2):331-8. doi: 10.1111/j.1365-2958.2006.05346.x.

15. Viollier PH, Thanbichler M, McGrath PT, West L, Meewan M, McAdams HH, et al. Rapid and sequential movement of individual chromosomal loci to specific subcellular locations during bacterial DNA replication. *Proc Natl Acad Sci U S A*. 2004 Jun 22;101(25):9257-62. doi: 10.1073/pnas.0402606101.

16. Deghelt M, Mullier C, Sternon JF, Francis N, Laloux G, Dotreppe D, et al. G1-arrested newborn cells are the predominant infectious form of the pathogen *Brucella abortus*. *Nat Commun*. 2014 Jul 9;5:4366. doi: 10.1038/ncomms5366.

17. Kahng LS, Shapiro L. Polar localization of replicon origins in the multipartite genomes of *Agrobacterium tumefaciens* and *Sinorhizobium meliloti*. *J Bacteriol*. 2003 Jun;185(11):3384-91. doi: 10.1128/JB.185.11.3384-3391.2003.

18. Frage B, Döhlemann J, Robledo M, Lucena D, Sobetzko P, Graumann PL, et al. Spatiotemporal choreography of chromosome and megaplasmids in the *Sinorhizobium meliloti* cell cycle. *Mol Microbiol*. 2016 Jun;100(5):808-23. doi: 10.1111/mmi.13351.

19. David A, Demarre G, Muresan L, Paly E, Barre FX, Possoz C. The two Cis-acting sites, *parS1* and *oriC1*, contribute to the longitudinal organisation of *Vibrio cholerae* chromosome I. *PLoS Genet*. 2014 Jul 10;10(7):e1004448. doi: 10.1371/journal.pgen.1004448.

20. Rasmussen T, Jensen RB, Skovgaard O. The two chromosomes of *Vibrio cholerae* are initiated at different time points in the cell cycle. *EMBO J*. 2007 Jul 11;26(13):3124-31. doi: 10.1038/sj.emboj.7601747.

21. Galibert F, Finan TM, Long SR, Puhler A, Abola P, Ampe F, et al. The composite genome of the legume symbiont *Sinorhizobium meliloti*. *Science*. 2001 Jul 27;293(5530):668-72. doi: 10.1126/science.1060966.

22. Cevallos MA, Cervantes-Rivera R, Gutiérrez-Ríos RM. The *repABC* plasmid family. *Plasmid*. 2008 Jul;60(1):19-37. doi: 10.1016/j.plasmid.2008.03.001.

23. Pinto UM, Pappas KM, Winans SC. The ABCs of plasmid replication and segregation. *Nat Rev Microbiol*. 2012 Nov;10(11):755-65. doi: 10.1038/nrmicro2882.

24. Cervantes-Rivera R, Pedraza-López F, Pérez-Segura G, Cevallos MA. The replication origin of a *repABC* plasmid. *BMC Microbiol*. 2011 Jun 30;11:158. doi: 10.1186/1471-2180-11-158.

25. Döhlemann J, Brennecke M, Becker A. Cloning-free genome engineering in *Sinorhizobium meliloti* advances applications of Cre/*loxP* site-specific recombination. *J Biotechnol*. 2016 Sep 10;233:160-70. doi: 10.1016/j.jbiotec.2016.06.033.

26. Tillier ER, Collins RA. The contributions of replication orientation, gene direction, and signal sequences to base-composition asymmetries in bacterial genomes. *J Mol Evol*. 2000 Mar;50(3):249-57. doi: 10.1007/s002399910029.

27. Lobry JR, Louarn JM. Polarisation of prokaryotic chromosomes. *Curr Opin Microbiol*. 2003 Apr;6(2):101-8. doi: 10.1016/s1369-5274(03)00024-9.

28. Necşulea A, Lobry JR. A new method for assessing the effect of replication on DNA base composition asymmetry. *Mol Biol Evol*. 2007 Oct;24(10):2169-79. doi: 10.1093/molbev/msm148.

29. Lam H, Matroule JY, Jacobs-Wagner C. The asymmetric spatial distribution of bacterial signal transduction proteins coordinates cell cycle events. *Dev Cell*. 2003 Jul;5(1):149-59. doi: 10.1016/s1534-5807(03)00191-6.

30. Hallez R, Bellefontaine AF, Letesson JJ, De Bolle X. Morphological and functional asymmetry in alpha-proteobacteria. *Trends Microbiol*. 2004 Aug;12(8):361-5. doi: 10.1016/j.tim.2004.06.002.

31. Sibley CD, MacLellan SR, Finan T. The *Sinorhizobium meliloti* chromosomal origin of replication. *Microbiology* (Reading). 2006 Feb;152(Pt 2):443-455. doi: 10.1099/mic.0.28455-0.

32. Hendrickson H, Lawrence JG. Selection for chromosome architecture in bacteria. *J Mol Evol*. 2006 May;62(5):615-29. doi: 10.1007/s00239-005-0192-2.

33. Livny J, Yamaichi Y, Waldor MK. Distribution of centromere-like *parS* sites in bacteria: insights from comparative genomics. *J Bacteriol*. 2007 Dec;189(23):8693-703. doi: 10.1128/JB.01239-07.

34. Cowie A, Cheng J, Sibley CD, Fong Y, Zaheer R, Patten CL, et al. An integrated approach to functional genomics: construction of a novel reporter gene fusion library for *Sinorhizobium meliloti*. *Appl Environ Microbiol*. 2006 Nov;72(11):7156-67. doi: 10.1128/AEM.01397-06.

35. Schäper S, Yau HCL, Krol E, Skotnicka D, Heimerl T, Gray J, et al. Seven-transmembrane receptor protein RgsP and cell wall-binding protein RgsM promote unipolar growth in *Rhizobiales*. *PLoS Genet*. 2018 Aug 13;14(8):e1007594. doi: 10.1371/journal.pgen.1007594.

36. Lau IF, Filipe SR, Søballe B, Økstad OA, Barre FX, Sherratt DJ. Spatial and temporal organization of replicating *Escherichia coli* chromosomes. *Mol Microbiol*. 2003 Aug;49(3):731-43. doi: 10.1046/j.1365-2958.2003.03640.x.

37. Mostafavi M, Lewis JC, Saini T, Bustamante JA, Gao IT, Tran TT, et al. Analysis of a taurine-dependent promoter in *Sinorhizobium meliloti* that offers tight modulation of gene expression. *BMC Microbiol*. 2014 Nov 25;14:295. doi: 10.1186/s12866-014-0295-2.

38. Ben-Yehuda S, Rudner DZ, Losick R. RacA, a bacterial protein that anchors chromosomes to the cell poles. *Science*. 2003 Jan 24;299(5606):532-6. doi: 10.1126/science.1079914.

39. Bowman GR, Comolli LR, Zhu J, Eckart M, Koenig M, Downing KH, et al. A polymeric protein anchors the chromosomal origin/ParB complex at a bacterial cell pole. *Cell*. 2008 Sep 19;134(6):945-55. doi: 10.1016/j.cell.2008.07.015.

40. Ebersbach G, Briegel A, Jensen GJ, Jacobs-Wagner C. A self-associating protein critical for chromosome attachment, division, and polar organization in *Caulobacter*. *Cell*. 2008 Sep 19;134(6):956-68. doi: 10.1016/j.cell.2008.07.016.

41. Yamaichi Y, Bruckner R, Ringgaard S, Möll A, Cameron DE, Briegel A, et al. A multidomain hub anchors the chromosome segregation and chemotactic machinery to the bacterial pole. *Genes Dev*. 2012 Oct 15;26(20):2348-60. doi: 10.1101/gad.199869.112.

42. Donovan C, Sieger B, Krämer R, Bramkamp M. A synthetic *Escherichia coli* system identifies a conserved origin tethering factor in Actinobacteria. *Mol Microbiol*. 2012 Apr;84(1):105-16. doi: 10.1111/j.1365-2958.2012.08011.x.

43. Buenemann M, Lenz P. A geometrical model for DNA organization in bacteria. *PLoS One*. 2010 Nov 3;5(11):e13806. doi: 10.1371/journal.pone.0013806.

44. Madras N, Orlitsky A, Shepp LA. Monte Carlo generation of self-avoiding walks with fixed endpoints and fixed length. *J Stat Phys***.** 1990 Jan; 58:159-183. doi: 10.1007/BF01020290.

45. Wang JD, Berkmen MB, Grossman AD. Genome-wide coorientation of replication and transcription reduces adverse effects on replication in *Bacillus subtilis*. *Proc Natl Acad Sci U S A*. 2007 Mar 27;104(13):5608-13. doi: 10.1073/pnas.0608999104.

46. Srivatsan A, Tehranchi A, MacAlpine DM, Wang JD. Co-orientation of replication and transcription preserves genome integrity. *PLoS Genet*. 2010 Jan 15;6(1):e1000810. doi: 10.1371/journal.pgen.1000810.

47. Ivanova D, Taylor T, Smith SL, Dimude JU, Upton AL, Mehrjouy MM, et al. Shaping the landscape of the *Escherichia coli* chromosome: replication-transcription encounters in cells with an ectopic replication origin. *Nucleic Acids Res*. 2015 Sep 18;43(16):7865-77. doi: 10.1093/nar/gkv704.

48. Milbredt S, Farmani N, Sobetzko P, Waldminghaus T. DNA replication in engineered *Escherichia coli* genomes with extra replication origins. *ACS Synth Biol*. 2016 Oct 21;5(10):1167-1176. doi: 10.1021/acssynbio.6b00064.

49. Bruhn M, Schindler D, Kemter FS, Wiley MR, Chase K, Koroleva GI, et al. Functionality of two origins of replication in *Vibrio cholerae* strains with a single chromosome. *Front Microbiol*. 2018 Nov 30;9:2932. doi: 10.3389/fmicb.2018.02932.

50. Val ME, Skovgaard O, Ducos-Galand M, Bland MJ, Mazel D. Genome engineering in *Vibrio cholerae*: a feasible approach to address biological issues. *PLoS Genet*. 2012 Jan;8(1):e1002472. doi: 10.1371/journal.pgen.1002472.

51. Val ME, Kennedy SP, Soler-Bistué AJ, Barbe V, Bouchier C, Ducos-Galand M, et al. Fuse or die: how to survive the loss of Dam in *Vibrio cholerae*. *Mol Microbiol*. 2014 Feb;91(4):665-78. doi: 10.1111/mmi.12483.

52. Hill TM, Pelletier AJ, Tecklenburg ML, Kuempel PL. Identification of the DNA sequence from the *E. coli* terminus region that halts replication forks. *Cell*. 1988 Nov 4;55(3):459-66. doi: 10.1016/0092-8674(88)90032-3.

53. Galli E, Ferat JL, Desfontaines JM, Val ME, Skovgaard O, Barre FX, et al. Replication termination without a replication fork trap. *Sci Rep*. 2019 Jun 5;9(1):8315. doi: 10.1038/s41598-019-43795-2.

54. Schlick T, Li B, Olson WK. The influence of salt on the structure and energetics of supercoiled DNA. *Biophys J*. 1994 Dec;67(6):2146-66. doi: 10.1016/S0006-3495(94)80732-5.

55. Wang X, Rudner DZ. Spatial organization of bacterial chromosomes. *Curr Opin Microbiol*. 2014 Dec;22:66-72. doi: 10.1016/j.mib.2014.09.016.

56. Badrinarayanan A, Le TB, Laub MT. Bacterial chromosome organization and segregation. *Annu Rev Cell Dev Biol*. 2015;31:171-99. doi: 10.1146/annurev-cellbio-100814-125211.

57. Osorio-Valeriano M, Altegoer F, Steinchen W, Urban S, Liu Y, Bange G, et al. ParB-type DNA segregation proteins are CTP-dependent molecular switches. *Cell*. 2019 Dec 12;179(7):1512-1524.e15. doi: 10.1016/j.cell.2019.11.015.

58. Ehrle HM, Guidry JT, Iacovetto R, Salisbury AK, Sandidge DJ, Bowman GR. Polar organizing protein PopZ is required for chromosome segregation in *Agrobacterium tumefaciens*. *J Bacteriol*. 2017 Aug 8;199(17):e00111-17. doi: 10.1128/JB.00111-17.

59. Grangeon R, Zupan JR, Anderson-Furgeson J, Zambryski PC. PopZ identifies the new pole, and PodJ identifies the old pole during polar growth in *Agrobacterium tumefaciens*. Proc Natl Acad Sci U S A. 2015 Sep 15;112(37):11666-71. doi: 10.1073/pnas.1515544112.

60. Robalino-Espinosa JS, Zupan JR, Chavez-Arroyo A, Zambryski P. Segregation of four *Agrobacterium tumefaciens* replicons during polar growth: PopZ and PodJ control segregation of essential replicons. *Proc Natl Acad Sci U S A*. 2020 Oct 20;117(42):26366-26373. doi: 10.1073/pnas.2014371117.

61. Fields AT, Navarrete CS, Zare AZ, Huang Z, Mostafavi M, Lewis JC, et al. The conserved polarity factor podJ1 impacts multiple cell envelope-associated functions in *Sinorhizobium meliloti*. *Mol Microbiol*. 2012 Jun;84(5):892-920. doi: 10.1111/j.1365-2958.2012.08064.x.

62. Lin L, Osorio Valeriano M, Harms A, Søgaard-Andersen L, Thanbichler M. Bactofilin-mediated organization of the ParABS chromosome segregation system in *Myxococcus xanthus*. *Nat Commun*. 2017 Nov 28;8(1):1817. doi: 10.1038/s41467-017-02015-z.

63. Ozaki S, Jenal U, Katayama T. Novel divisome-associated protein spatially coupling the Z-Ring with the chromosomal replication terminus in *Caulobacter crescentus*. *mBio*. 2020 Apr 28;11(2):e00487-20. doi: 10.1128/mBio.00487-20.

64. Woldemeskel SA, McQuillen R, Hessel AM, Xiao J, Goley ED. A conserved coiled-coil protein pair focuses the cytokinetic Z-ring in *Caulobacter crescentus*. *Mol Microbiol*. 2017 Sep;105(5):721-740. doi: 10.1111/mmi.13731.

65. Zimmerman SB, Trach SO. Estimation of macromolecule concentrations and excluded volume effects for the cytoplasm of *Escherichia coli*. *J Mol Biol*. 1991 Dec 5;222(3):599-620. doi: 10.1016/0022-2836(91)90499-v.

66. Zimmerman SB, Minton AP. Macromolecular crowding: biochemical, biophysical, and physiological consequences. *Annu Rev Biophys Biomol Struct*. 1993;22:27-65. doi: 10.1146/annurev.bb.22.060193.000331.

67. Parry BR, Surovtsev IV, Cabeen MT, O'Hern CS, Dufresne ER, Jacobs-Wagner C. The bacterial cytoplasm has glass-like properties and is fluidized by metabolic activity. *Cell*. 2014 Jan 16;156(1-2):183-94. doi: 10.1016/j.cell.2013.11.028.

68. De Nisco NJ, Abo RP, Wu CM, Penterman J, Walker GC. Global analysis of cell cycle gene expression of the legume symbiont *Sinorhizobium meliloti*. *Proc Natl Acad Sci U S A*. 2014 Mar 4;111(9):3217-24. doi: 10.1073/pnas.1400421111.

69. diCenzo GC, Cangioli L, Nicoud Q, Cheng JHT, Blow MJ, Shapiro N, et al. DNA Methylation in *Ensifer* species during free-living growth and during nitrogen-fixing symbiosis with *Medicago* spp. *mSystems*. 2022 Feb 22;7(1):e0109221. doi: 10.1128/mSystems.01092-21.

70. Fioravanti A, Fumeaux C, Mohapatra SS, Bompard C, Brilli M, Frandi A, et al. DNA binding of the cell cycle transcriptional regulator GcrA depends on N6-adenosine methylation in *Caulobacter crescentus* and other Alphaproteobacteria. *PLoS Genet*. 2013 May;9(5):e1003541. doi: 10.1371/journal.pgen.1003541.

71. Haakonsen DL, Yuan AH, Laub MT. The bacterial cell cycle regulator GcrA is a σ70 cofactor that drives gene expression from a subset of methylated promoters. *Genes Dev*. 2015 Nov 1;29(21):2272-86. doi: 10.1101/gad.270660.115.

72. Wright R, Stephens C, Shapiro L. The CcrM DNA methyltransferase is widespread in the alpha subdivision of proteobacteria, and its essential functions are conserved in *Rhizobium meliloti* and *Caulobacter crescentus*. *J Bacteriol*. 1997 Sep;179(18):5869-77. doi: 10.1128/jb.179.18.5869-5877.1997.

73. Gueiros-Filho FJ, Losick R. A widely conserved bacterial cell division protein that promotes assembly of the tubulin-like protein FtsZ. *Genes Dev*. 2002 Oct 1;16(19):2544-56. doi: 10.1101/gad.1014102.

74. Ozaki S, Wakasugi Y, Katayama T. Z-Ring-associated proteins regulate clustering of the replication terminus-binding protein ZapT in *Caulobacter crescentus*. *mBio*. 2021 Jan 26;12(1):e02196-20. doi: 10.1128/mBio.02196-20.

75. Ulvé VM, Sevin EW, Chéron A, Barloy-Hubler F. Identification of chromosomal alpha-proteobacterial small RNAs by comparative genome analysis and detection in *Sinorhizobium meliloti* strain 1021. *BMC Genomics*. 2007 Dec 19;8:467. doi: 10.1186/1471-2164-8-467.

76. Brilli M, Fondi M, Fani R, Mengoni A, Ferri L, Bazzicalupo M, et al. The diversity and evolution of cell cycle regulation in alpha-proteobacteria: a comparative genomic analysis. *BMC Syst Biol*. 2010 Apr 28;4:52. doi: 10.1186/1752-0509-4-52.

77. Biondi EG, Reisinger SJ, Skerker JM, Arif M, Perchuk BS, Ryan KR, et al. Regulation of the bacterial cell cycle by an integrated genetic circuit. *Nature*. 2006 Dec 14;444(7121):899-904. doi: 10.1038/nature05321.

78. Chen YE, Tsokos CG, Biondi EG, Perchuk BS, Laub MT. Dynamics of two Phosphorelays controlling cell cycle progression in *Caulobacter crescentus*. *J Bacteriol*. 2009 Dec;191(24):7417-29. doi: 10.1128/JB.00992-09.

79. Mann TH, Seth Childers W, Blair JA, Eckart MR, Shapiro L. A cell cycle kinase with tandem sensory PAS domains integrates cell fate cues. *Nat Commun*. 2016 Apr 27;7:11454. doi: 10.1038/ncomms11454.

80. Mann TH, Shapiro L. Integration of cell cycle signals by multi-PAS domain kinases. *Proc Natl Acad Sci U S A*. 2018 Jul 24;115(30):E7166-E7173. doi: 10.1073/pnas.1808543115.

81. Narayanan S, Kumar L, Radhakrishnan SK. Sensory domain of the cell cycle kinase CckA regulates the differential DNA binding of the master regulator CtrA in *Caulobacter crescentus*. *Biochim Biophys Acta Gene Regul Mech*. 2018 Oct;1861(10):952-961. doi: 10.1016/j.bbagrm.2018.08.006.

82. Bertani G. Studies on lysogenesis. I. The mode of phage liberation by lysogenic *Escherichia coli*. *J Bacteriol*. 1951 Sep;62(3):293-300. doi: 10.1128/jb.62.3.293-300.1951.

83. Green MR, Hughes H, Sambrook J, MacCallum P. Molecular cloning: a laboratory manual, 4th ed., Cold Spring Harbor Laboratory Press, New York; Cold Spring Harbor; 4th ed; 2012. 1890 p

84. Beringer JE. R factor transfer in *Rhizobium leguminosarum*. *J Gen Microbiol*. 1974 Sep;84(1):188-98. doi: 10.1099/00221287-84-1-188.

85. Zhan HJ, Lee CC, Leigh JA. Induction of the second exopolysaccharide (EPSb) in *Rhizobium meliloti* SU47 by low phosphate concentrations. *J Bacteriol*. 1991 Nov;173(22):7391-4. doi: 10.1128/jb.173.22.7391-7394.1991.

86. Simon R, Priefer U, Pühler A. A broad host range mobilization system for *in vivo* genetic engineering: transposon mutagenesis in Gram negative bacteria. *Nat Biotechnol*. 1983 Nov;1(9):784-791. doi: 10.1038/nbt1183-784.

87. Ferri L, Gori A, Biondi EG, Mengoni A, Bazzicalupo M. Plasmid electroporation of *Sinorhizobium* strains: the role of the restriction gene *hsdR* in type strain Rm1021. *Plasmid*. 2010 May;63(3):128-35. doi: 10.1016/j.plasmid.2010.01.001.

88. Schäfer A, Tauch A, Jäger W, Kalinowski J, Thierbach G, Pühler A. Small mobilizable multi-purpose cloning vectors derived from the *Escherichia coli* plasmids pK18 and pK19: selection of defined deletions in the chromosome of *Corynebacterium glutamicum*. *Gene*. 1994 Jul 22;145(1):69-73. doi: 10.1016/0378-1119(94)90324-7.

89. Checcucci A, diCenzo GC, Ghini V, Bazzicalupo M, Becker A, Decorosi F, et al. Creation and characterization of a genomically hybrid strain in the nitrogen-fixing symbiotic bacterium *Sinorhizobium meliloti*. *ACS Synth Biol*. 2018 Oct 19;7(10):2365-2378. doi: 10.1021/acssynbio.8b00158.

90. Schäper S, Krol E, Skotnicka D, Kaever V, Hilker R, Søgaard-Andersen L, et al. Cyclic Di-GMP regulates multiple cellular functions in the symbiotic Alphaproteobacterium *Sinorhizobium meliloti*. *J Bacteriol*. 2015 Nov 16;198(3):521-35. doi: 10.1128/JB.00795-15.

91. McGee-Russell SM, Allen RD. Reversible stabilization of labile microtubules in the reticulopodial network of *Allogromia*. *Adv Cell Mol Biol*. 1971;1:153-184.

92. Ducret A, Quardokus EM, Brun YV. MicrobeJ, a tool for high throughput bacterial cell detection and quantitative analysis. *Nat Microbiol*. 2016 Jun 20;1(7):16077. doi: 10.1038/nmicrobiol.2016.77.

93. Marchler-Bauer A, Lu S, Anderson JB, Chitsaz F, Derbyshire MK, DeWeese-Scott C, et al. CDD: a conserved domain database for the functional annotation of proteins. *Nucleic Acids Res*. 2011 Jan;39(Database issue):D225-9. doi: 10.1093/nar/gkq1189.

94. Marchler-Bauer A, Derbyshire MK, Gonzales NR, Lu S, Chitsaz F, Geer LY, et al. CDD: NCBI's conserved domain database. *Nucleic Acids Res*. 2015 Jan;43(Database issue):D222-6. doi: 10.1093/nar/gku1221.

95. Marchler-Bauer A, Bo Y, Han L, He J, Lanczycki CJ, Lu S, et al. CDD/SPARCLE: functional classification of proteins via subfamily domain architectures. *Nucleic Acids Res*. 2017 Jan 4;45(D1):D200-D203. doi: 10.1093/nar/gkw1129.

■ FIGURE CAPTIONS

Fig 1. Design and compositional properties of the genomic content in *S. meliloti* replicon fusion strains SmAB and SmABC.
(A) Configurations of replicon fusions. The inner concentric ring represents the deviation (positive: grey colored, negative: black colored) from the average GC-skew of the entire sequence calculated by a sliding window of (G-C)/(G+C). Replication origin of pSymA, pSymB and the chromosome (red circles including A/B/C); predicted terminus region of pSymA, pSymB and the chromosome (black diamonds including A/B/C); chromosome (Chr); pSymAB (AB); fusion product of pSymAB and the chromosome (ABC). **(B)** Pulsed-field gel electrophoresis of PacI digested gDNA from *S. meliloti* strains SmCreΔhsdR (Wt), SmAB (AB) and SmABC (ABC). Expected banding pattern for SmCreΔhsdR (wt): 3.65 Mbp (chromosome), 1.35 Mbp (pSymA), 1.15 Mbp (pSymB fragment 1), 0.53 Mbp (pSymB fragment 2). SmAB: 3.65 Mbp (chromosome), 1.67 Mbp, 0.83 Mbp, 0.53 Mbp. SmABC: 2.53 Mbp, 1.94 Mbp, 1.67 Mbp, 0.53 Mbp. M: PFGE marker yeast chromosomes, *Saccharomyces cerevisiae* (Strain YNN295). **(C)** Cumulated CDS skew (CDS^c skew) curve represents the coding sequence orientation bias in the SmABC fusion strain. **(D)** KOPS distribution in SmABC. For the analysis and representation of the replicon structure the *E. coli* KOPS consensus sequence (GGGNAGGG) was used. $KOPS^c$ visualizes the accumulation of the KOPS motifs either located on the forward strand (black lines) or on the reverse strand (grey lines) of the sequence in SmABC. Color code: chromosome (grey), pSymA (green), pSymB (blue).

Fig 2. Basic characterization of *S. meliloti* replicon fusion strains SmAB and SmABC.
(A) Phase contrast microscopy images of SmAB, SmABC and precursor strain SmCreΔhsdR (wt) representative cells at different stages of the cell cycle. Scale bar: 2 µm. **(B)** Growth of *S. meliloti* SmAB and SmABC compared to precursor strain SmCreΔhsdR (wt) in rich medium (TY), minimal medium (MOPS low P_i), high salt medium (TY + 0.4 M NaCl) and high sucrose medium (TY + 0.5 M sucrose). Data represent the mean ± standard deviation of three technical replicates. Growth curves of biological replicates are shown in S8A Fig.

Fig 3. Deletion and mutational studies in *S. meliloti* SmCreΔhsdR (wt), SmAB and SmABC fusion strains.
(A) Growth curves of *S. meliloti* SmAB and SmABC *repC* deletion strains. Prior to inoculation, overnight cultures were washed with 0.9 % NaCl and adjusted to an OD_{600} ~ 0.15 in TY medium. Mean and standard deviation was calculated from three technical replicates. **(B)** Morphology of the double *repC* deletion mutant strain SmABCΔoriV. **(C)** Marker frequency analysis of SmABC and SmABCΔoriV of logarithmic (OD_{600} of 0.6) vs. stationary (OD_{600} of 2.6) cultures. Trimmed and normalized marker frequencies are depicted in log2 as a function of the genome position in Mbp. Arrowheads indicate the position of origin and predicted terminus regions [32]. Note that SmABCΔoriV lacks *oriA* and *oriB* due to *repC* deletions (Δ*oriA* and Δ*oriB*).

Fig 4. Investigation and modeling of the spatial DNA organization in SmABCΔR.
(A) Schematic true to scale representation of the SmABCΔR monopartite genome with *tetO* and *lacO* integration sites 1-18 selected to reveal the spatial configuration of the genomic DNA. Color code: chromosome (grey), pSymA (green), pSymB (blue). Red circles: replication origins, black diamonds: terminus regions. **(B)** Example of snapshot

images from labeled cells used for the 2D genome mapping study. Scale bar: 1 µm. **(C)** Normalized spatial localization of labeled loci within SmABCΔR (filled circles) compared to SmCreΔhsdR (non-filled circles) with wild type genome configuration as a function of the genome sequence coordinate. Old cell pole: 1, New cell pole: -1. **(D)** Scatter plots of selected strains illustrate examples of similar (Pos. no.: 2, 3, 18) and clearly different distribution (Pos. no.: 5, 10, 16) of marked loci within SmABCΔR (red dots) and SmCreΔhsdR (black dots). **(E)** Example configuration of simulations consolidating physical principles such as self-avoidance and compaction of DNA in a SmABCΔR cell represented as sphero-cylindrical shape. **(F)** Model of DNA self-organization in SmABCΔR compared to the experimental data. The model considers a spatial confinement (experimental standard deviation) for *terA* and *terB* in addition to *oriABC* and *terC* as fixpoints. Shown are the normalized locations in the cell as a function of the position on the genomic map. Experimental data of origins are indicated by red circles, terminus regions by black diamonds and remaining marker positions with non-filled circles. The red line depicts the model results averaged over 276 cells. Shaded areas represent the standard deviations. For the model a cell of 1800 nm and a loop-size of 1298 bp (DNA within a "blob") was used.

Fig 5. Spatiotemporal pattern of origin and terminus regions in native and reorganized multi-replicon backgrounds.

(A) Temporal order of origin and terminus region segregation in SmCreΔhsdR (wt), SmABΔR (AB), SmABCΔR (ABC) and SmABCΔoriVΔR (ABCΔ). Colored bars with a black center indicate the standard deviation and the mean timepoint of sister foci separation within the cell cycle normalized to 100 %. Analyzed M-cells: 20 (*oriC*), 10 (*oriA/B*) and 5 (*terA/B/C*). **(B)** Localization of *ori* and *ter* foci segregation in SmCreΔhsdR (wt), SmABΔR, SmABCΔR and SmABCΔoriVΔR. The bar chart depicts the relative longitudinal position of a single focus before separation within the normalized cell (old pole: 0, new pole: 1, midcell: 0,5). Data represent the mean ± the standard deviation for *oriC* (n=20), *terC* (n=5), *oriA* (n=10), *terA* (n=5), *oriB* (n=10) and *terB* (n=5) in M-cells. **(C)** Spatiotemporal choreography of *oriC* and *terC* in SmCreΔhsdR (wt), SmABΔR, SmABCΔR and SmABCΔoriVΔR. (i) Time lapse series with *oriC* (ParB-cerulean) and *terC* (TetR-mVenus) in SmCreΔhsdR (wt) and SmABCΔR. Scale bar: 1 µm. (ii) Timepoint of *oriC* (cyan circles) arriving at the new cell pole in relation to *terC* (yellow circles) release from the same pole within a normalized cell cycle (0-100 %). Analyzed M-cells: 5 each. Black bar indicates the data mean. **(D)** Time lapse microscopy series of SmCreΔhsdR (wt) and SmABCΔR as examples of sequential segregation of *oriA* and *oriB* with varying order. Arrowheads depict the position of segregation start. **(E)** Percentage of cells with *oriA* foci (green) and *oriB* foci (blue) segregating first. Cells analyzed: SmCreΔhsdR (wt) (n=172), SmABΔR (n=179), SmABCΔR (n=169), and SmABCΔoriVΔR (n=197).

Color code: chromosome (grey), pSymA (green), pSymB (blue). Mother cell (M), daughter cell (D). Note that SmABCΔoriVΔR lacks *oriA* and *oriB* due to *repC* deletions. For simplicity, localization of *repABΔC* loci is denoted as *oriA* and *oriB* in panels A, B, C and E.

Fig 6. Mislocalization of the replication origin regions in SmABCΔoriVΔR.

(A) Localization of *oriC* in SmCreΔhsdR (wt), SmABΔR, SmABCΔR and SmABCΔoriVΔR G_1-phase cells. Bar chart depict the percentage of cells with *oriC* (ParB-cerulean) foci at the cell poles (white cell compartment, 0.5 to 1 and -

0.5 to -1) and at midcell (grey cell compartment, 0.5 to -0.5). Cells analyzed: SmCreΔhsdR (wt) (n=480), SmABΔR (n=581), SmABCΔR (n=371), SmABCΔoriVΔR (n=936). **(B)** Co-localization of *oriA/B/C* in SmCreΔhsdR (wt), SmABΔR, SmABCΔR and SmABCΔoriVΔR G_1-phase cells. Shown are the percentage of cells with localization of either *oriA/C* (white bar), *oriB/C* (grey bar) and *oriA/B/C* (black bar) in the midcell area (0.5 to -0.5). Cells analyzed: SmCreΔhsdR (wt) (n=639), SmABΔR (n=460), SmABCΔR (n=405), SmABCΔoriVΔR (n=246). Dots in the schematic cells represent *oriC* (grey), *oriA* (green) and *oriB* (blue). Note that SmABCΔoriVΔR lacks *oriA* and *oriB* due to *repC* deletions. For simplicity, localization of *repABΔC* loci is denoted as *oriA* and *oriB*. **(C)** Analysis of *oriC* localization in predivisional cells of SmABCΔoriVΔR. The density map indicates the position of the chromosomal origin in sibling 1 (left cell) and sibling 2 (right cell) of predivisional cells (n=400) in a normalized scale. Snapshot images and percentage of the two major *oriC* spatial position patterns in predivisional cells. Scale bar: 2 µm. **(D)** Time lapse microscopy series of generic *oriC* choreography in sibling cells of SmABCΔoriVΔR. Arrowheads depict the position of visible *oriC* foci segregation. Scale bar: 1µm. **(E)** Model of *oriC* choreography in SmABCΔoriVΔR. The model differentiates between *oriC* coordination in daughter (D, light grey) and mother (M, anthracite) cells. Cyan cycles with numbers (1: *oriC1*, 2: *oriC2*) represent the deduced *oriC* positioning within the cells.

Fig 7. Localization of the chromosomal origin in fusion strains with wild type CckA and CckA^{R436H}.

(A) Localization of *oriC* (ParB-cerulean) in SmCreΔhsdR (wt) and SmABCΔR G_1-phase cells with $cckA_{R436H}$ (black bars) compared to respective strains with wild type *cckA* (grey shaded bars). Cells analyzed: SmCreΔhsdR n= 480 ($cckA_{wt}$), n=407 ($cckA_{R436H}$), SmABCΔR n= 371 ($cckA_{wt}$), n=352 ($cckA_{R436H}$). Snapshot images as example for polar and midcell localization of *oriC*. Scale bar: 1 µm. **(B)** Comparison of polar and midcell localization of *oriC* in SmABCΔoriV (precursor of SmABCΔoriVΔR) and SmABC, both with wild type *cckA*. White bars depict the percentage of cells with polar *oriC* localization whereas grey bars represent midcell localization. Cells analyzed: SmABCΔoriV (n= 472), SmABC (n=584).

■ FIGURES

Fig1

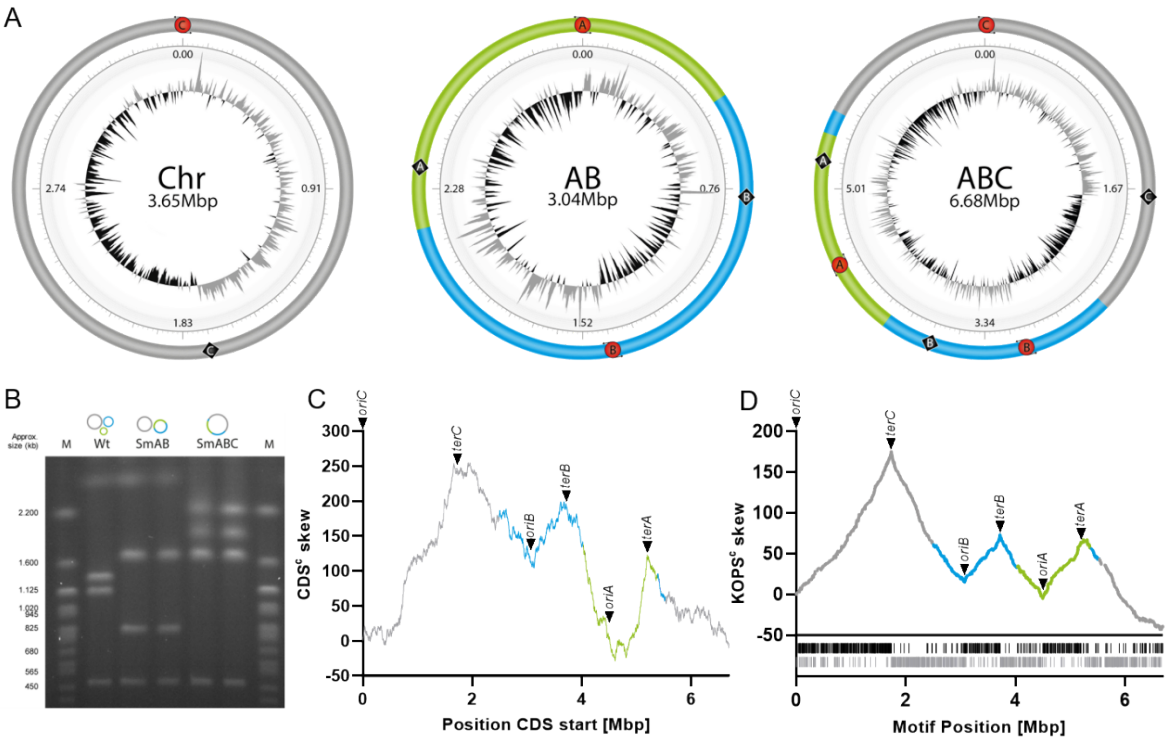

1126 **Fig2**

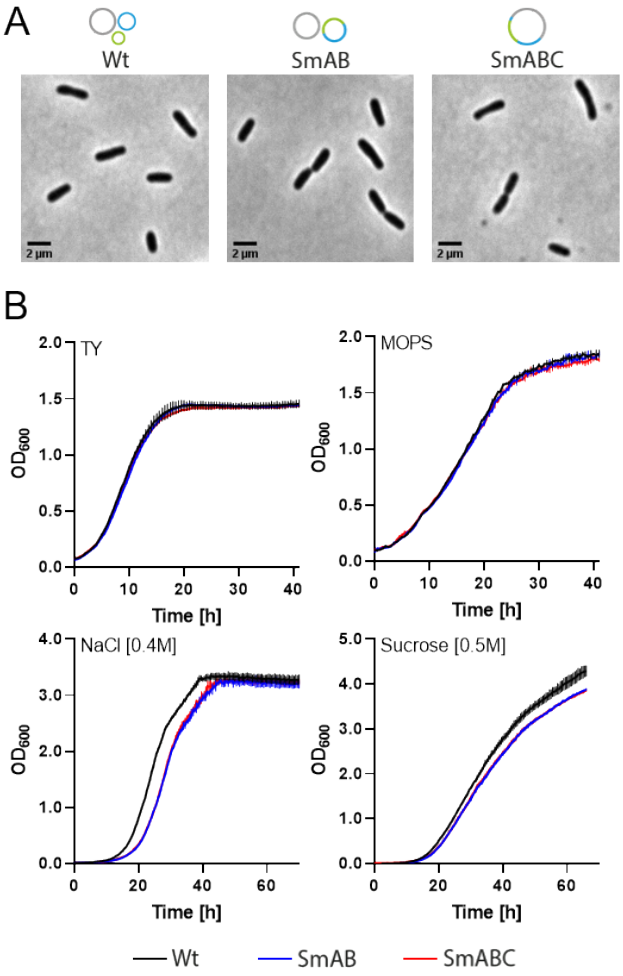

1127

1128 **Fig3**

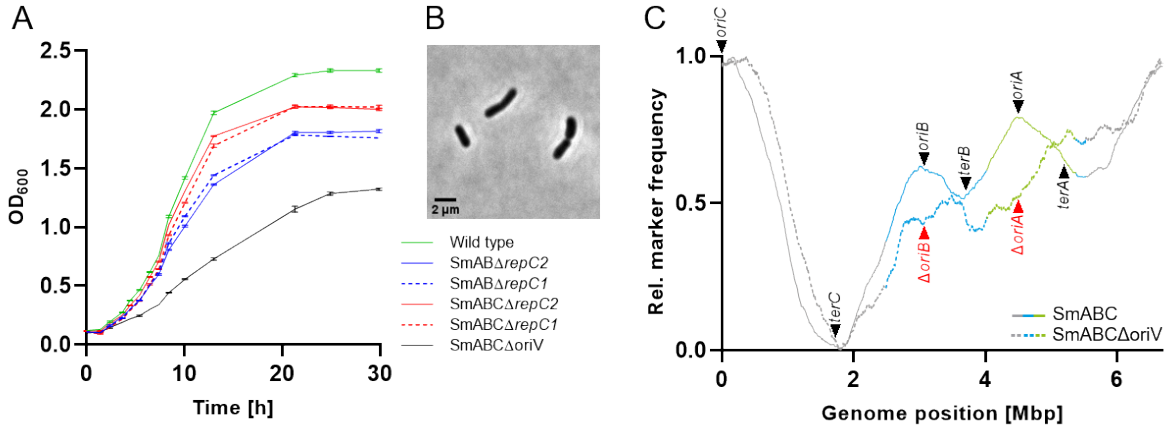

1129

Fig4

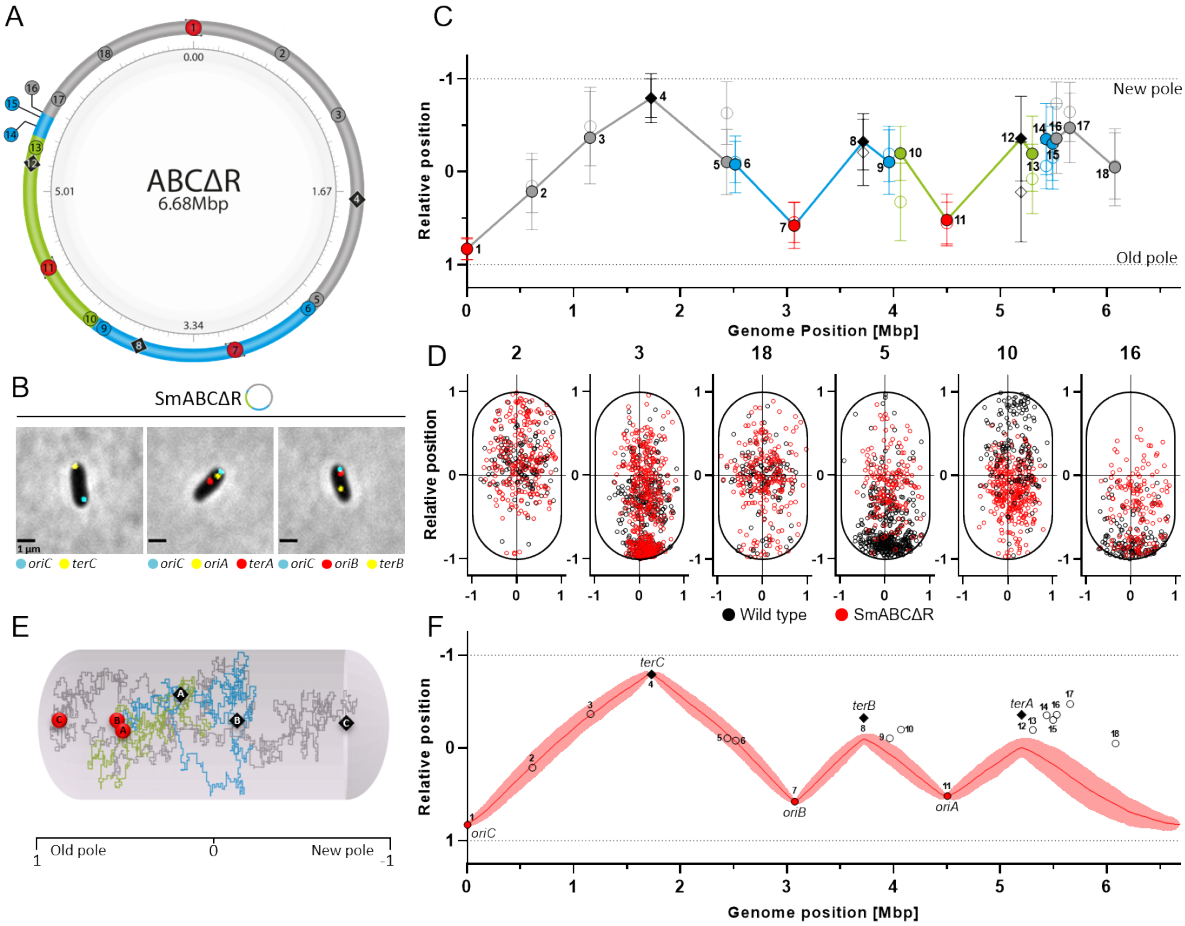

1132 **Fig5**

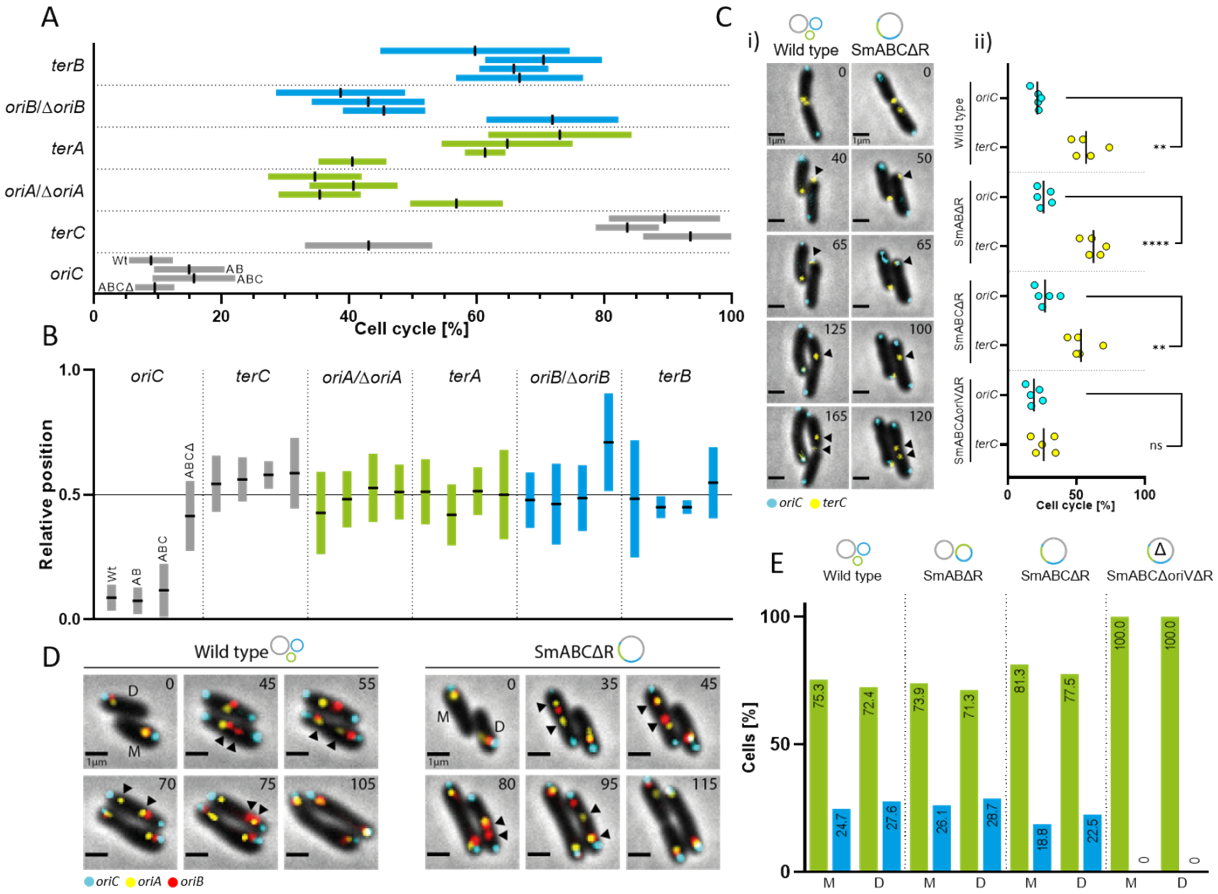

1133

1134

1135 **Fig6**

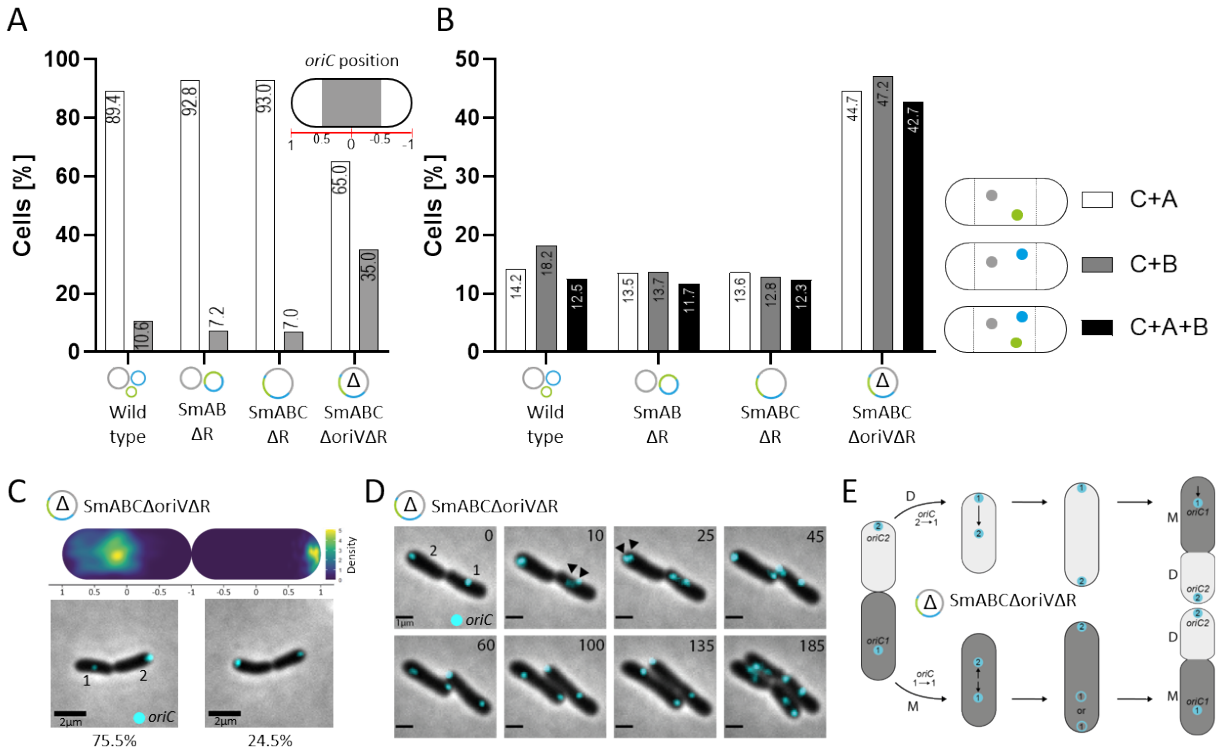

1136

1137

1138 **Fig7**

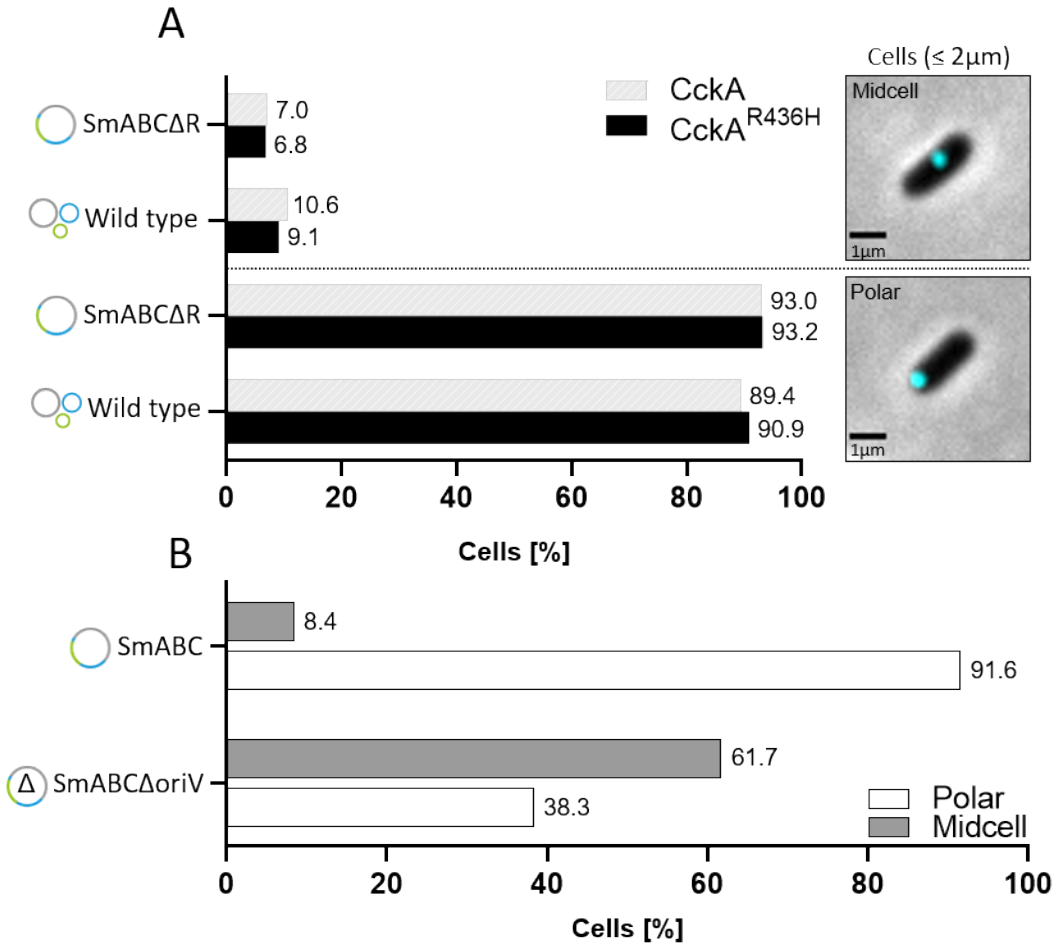

1139

■ SUPPORTING INFORMATION

S1 Fig. Construction of *S. meliloti* SmAB and SmABC. (A) Initially, *S. meliloti* SmCreΔhsdR (wild type) was transformed with integrative pK18mobsacB derivatives pJD98 and pJD99, thereby providing *loxL* and *loxR* sites (black triangles, non-filled indicates mutation) at 125°(pSymA) and 169°(pSymB) for Cre-mediated megaplasmid fusion and components of a spectinomycin resistance cassette allowing for positive selection after Cre/*lox* recombination. Plasmid backbone of pJD99 was deleted via *sacB* mediated sucrose selection. In contrast, the backbone of pJD98 was retained for enabling sucrose selection in a later step. Due to Cre-mediated replicon fusion, the homologous *nodPQ1*(SMa0855/SMa0857) and *nodPQ2* (SMb21223/SMb21224) operon came into close proximity, flanking the pJD98 derived plasmid backbone, thereby enabling sucrose selection-mediated deletion of the vector backbone and a wild type *loxP* site (resulting from *loxL/R* mediated Cre recombination). Thus, the resulting strain SmAB could be easily used for further Cre/*lox* reactions. P_{aacC1}: Constitutive resistance cassette promoter. **(B)** *S. meliloti* strain SmAB was then transformed with pK18mobsacB derivative pJD130 which provides the hybrid replicon pSymAB with a *loxL* site at 238° followed by the constitutive promoter P*min2*. Sucrose selection-mediated deletion of the plasmid backbone resulted in strain JDSm111 which was then transformed with pJD126. In this way the chromosome was equipped with a *loxR* site at 246° and the promoterless gentamicin resistance gene *aacC1*, thereby allowing for selection on gentamicin resistance after Cre/*lox* recombination. Thus, the resulting strain SmABC exhibited an entirely merged genome and antibiotic resistances against tetracycline, spectinomycin and gentamicin. *lox* sites were integrated close to the *algI* homologs of pSymB (SMb20843) and the chromosome (SMc01551), thereby enabling sucrose selection-mediated deletion of a remaining *loxP* site and the plasmid backbone. *A/B/C*: DNA replication origin/terminus region of pSymA/pSymB/chromosome. Mbp: Megabase pairs. R: antibiotic resistance gene.

S2 Fig. Transition zone validation in SmAB, SmABC and precursor strains. (A) Successful merging of pSymA and pSymB was initially verified using PCR. Amplification of a DNA segment covering the *loxP* fusion site 1 (FS1) with primer 239/131 (blue arrows, fragment size: 0.76 kb) was only possible for strain JDSm98 (2) after Cre/*lox*-mediated fusion and sucrose selection. In turn and as expected, this primer combination did not lead to an amplicon in the pre-fusion strain JDSm97 (1) and not in the final secondary replicon fusion strains SmAB R1 (4) and SmAB R2 (3) after locking the genomic design by sucrose selection-mediated removal of the pJD98 vector backbone including the wild type *loxP* and primer binding site. Using primer 236/249 (red arrows, fragment size: 1.68 kb) targeting fusion site 2 (FS2) including the mutated *loxLR* site, PCR amplification was achieved for strains JDSm98 (2), SmAB R1 (4) and SmAB R2 (3) but not for JDSm97 (1). (**B)** Proper fusion between the chromosome and pSymAB was validated using PCR amplification of the fusion site 3 (FS3) for strain JDSm121 (6), SmABC R1 (8) and SmABC R2 (7) with primer 360/247 (green arrows, fragment size: 1.18kb), but not for the pre-fusion strain JDSm118 (5). Fusion at site 4 (FS4) was confirmed with primer 363/131 (orange arrows, fragment size: 0.80 kb) for strain JDSm121 (6). As expected, no amplification with this primer combination could be achieved for the pre-fusion strain JDSm118 (5) and the final SmABC strains (7/8) with removed pJD126 backbone including the wild type *loxP* and primer binding site.

S3 Fig. Replichore ratio in *S. meliloti* fusion strains. (A) Predicted replicon structure and replichore distribution in SmCreΔhsdR (wt), SmAB and SmABC. Dashed arrows with circular basis depict the predicted bidirectional replication movement of the individual replichores emerging from *oriC*, *oriA* and *oriB*. **(B)** Percentage ratio between the left (black) and right (grey) replichores of the chromosome (Chr) and secondary replicons in *S. meliloti* wild type, SmAB and SmABC. Red circles with A/B/C: replication origin of pSymA/pSymB/chromosome, Black diamonds with A/B/C: predicted terminus of pSymA/pSymB/ chromosome.

S4 Fig. Visualization of the asymmetric nucleotide composition in SmCreΔhsdR (wt), SmAB and SmABC. The abundance of nucleotides is represented by the GC skew value of each replicon sequence. Analyzed sequences were subdivided into 1000 parts (windows) and the GC skew was calculated for each window as (G – C) / (G + C). The GC skew graph depicts the value of individual windows at certain positions moving with a defined step size along the analyzed sequence. The cumulative GC skew (GC^C skew) was calculated by addition of all GC-values from adjacent windows up to a specific position thereby most likely representing the replichore bias with minimum values at origin and maximum values at terminus regions. The underlying nucleotide skew data were generated using GenSkew (http://genskew.csb.univie.ac.at). Analysis parameter: SmCreΔhsdR (Chromosome): GC-content: 62.7 %, window and step size: 3650 bp, max. GC^C value: 6.44 (Pos: 1.73 Mbp), min. GC^C value: -3.94 (3.65 Mbp). SmCreΔhsdR (pSymA): GC-content: 60.4 %, window and step size: 1354 bp, max. GC^C value: 3.16 (Pos: 0.55 Mbp), min. GC^C value: -3.29 (1.35 Mbp). SmCreΔhsdR (pSmyB): GC-content: 62.4 %, window and step size: 1686 bp, max. GC^C value: 6.65 (Pos: 1.10 Mbp), min. GC^C value: -0.64 (0.05 Mbp). SmAB (pSymAB): GC-content: 61.5 %, window and step size: 3038 bp, max. GC^C value: 3.02 (Pos: 2.23 Mbp), min. GC^C value: -0.06 (1.43 Mbp). SmABC (Chr. + pSymAB): GC-content: 62.2 %, window and step size: 6683 bp, max. GC^C value: 3.52 (Pos: 1.74 Mbp), min. GC^C value: -2.23 (6.68 Mbp). Positions of terminus regions are based on architecture imparting motif sequence (AIMS) predictions (Hendrickson & Lawrence, 2006). Color code: Chromosome (grey), pSymA (green), pSymB (blue).

S5 Fig. Gene orientation bias in SmCreΔhsdR (wt), SmAB and SmABC. The number of coding sequences (CDS) located on the individual replicons revealed a gene strand bias between the leading (solid line) and the lagging (dashed line) strand of a replichore with genes predominantly accumulating on the leading strand. SmCreΔhsdR (wt) Chr: 1871 CDS (56 %) on the leading and 1488 CDS (44 %) on the lagging strand, pSymA: 787 CDS (61 %) on the leading and 503 CDS (39 %) on the lagging strand, pSymB: 918 CDS (58 %) on the leading and 669 CDS (42 %) on the lagging strand. SmAB (pSymAB): 1691 CDS (59 %) on the leading and 1183 CDS (41 %) on the lagging strands. SmABC (ABC): 3562 CDS (57 %) on the leading and 2666 CDS (43 %) on

the lagging strands. Terminus regions depicted as predicted by Hendrickson & Lawrence, 2006. Color code: Chromosome (grey), pSymA (green), pSymB (blue). *oriA*/*B*/*C*: origin of replication, *terA*/*B*/*C*: terminus region.

S6 Fig. Oligonucleotide bias of FtsK orienting polar sequences (KOPS). Count of the *E. coli* KOPS consensus motif GGGNAGGG (Bigot et al., 2005) on the forward (filled circels) and complementary strand (non-filled circles) respectively is depicted as a function of the position on the genome sequence. The KOPS sequence as an architecture imparting motif was used to display the strand asymmetry bias on the individual replichores. KOPS distribution was analysed by use of fuzznuc (http://emboss.toulouse.inra.fr/cgi-bin/emboss/fuzznuc?_pref_hide_optional=1). Terminus regions depicted as predicted by Hendrickson & Lawrence, 2006. Color code: Chromosome (grey), pSymA (green), pSymB (blue). *oriA*/*B*/*C*: origin of replication, *terA*/*B*/*C*: terminus region. Mbp: megabase pairs.

S7 Fig. Cell shape of SmCreΔhsdR (wt), SmAB, SmABC in TY and TY with 0.4M NaCl. (A) Microscopic snapshot analysis revealed a small subpopulation of cells with misplaced division septum (orange arrowhead) probably resulting in coccus-shaped cell types here termed as minicells (red arrowhead). Scale bar: 2 µm. **(B)** Scatter plot with cell length [µm] as a function of cell area [µm^2] demonstrate the size distribution of SmCreΔhsdR (wt), SmAB and SmABC strains in an exponential growth phase culture. The proportion of minicells defined with cell length <1 µm and area <0.6 µm^2 is indicated by the red square. **C:** Percentage of minicells in TY with wt: 0.15 % ([n=1958), SmAB: 0.16 % (n=2501), SmABC 0,15 % (n=1989) and TY [0.4 M NaCl] with wt: 0.04 % (n=2739), SmAB: 0.3 % (n=1687), SmABC: 0.08 % (n=2395).

S8 Fig. Growth of SmCreΔhsdR (wt), SmAB and SmABC. **(A)** Growth of SmAB and SmABC replicate 2 compared to the precursor strain SmCreΔhsdR (wt) with wild type genome configuration as a control in rich medium (TY), low phosphate minimal medium (MOPS) and TY supplemented with either 0.4 M NaCl or 0.5 M sucrose. **(B)** Hypersaline (0.6 M NaCl) and high sugar (0.7 M sucrose) condition revealed an increasing negative effect on growth behavior for strains SmAB and SmABC. However, even SmCreΔhsdR with wild type-like genome configuration exhibit a diminished growth capacity under this stress conditions. For the analysis, cell cultures were grown for 40 h and 70 h, respectively at 30 °C under shaking conditions (200 rpm). Optical density was measured every 30 minutes at 600 nm (OD_{600}). Prior to inoculation, overnight cultures were washed with 0.9 % NaCl and adjusted to an OD_{600} ~ 0.01 (TY+ 0.4 M NaCl, TY+ 0.5 M and 0.7 M sucrose) or 0.1 (TY, MOPS and TY+ 0.6 M NaCl) in respective media supplemented with 600 µg/ml streptomycin. Error bars indicate standard deviation calculated from three technical replicates.

S9 Fig. Deletion of *oriC*. Previously, putative DnaA boxes 2-4 were identified to be essential for functionality of a minimal chromosome origin (Sibley et al., 2006). Moreover, the transcription start site of *hemE* has been determined (Schlüter et al., 2013) allowing for prediction of respective promoter motifs. In order to test whether the *oriC* region can be deleted when the genome is entirely merged, *S. meliloti* SmABC was transformed with deletion constructs pJD226-228 and *sacB* mediated sucrose selection was performed. However, clones lacking regions Δ1 (genome position smc3654130-smc283), Δ2 (smc3654130-smc478) or Δ3 (smc292-smc478) could not be identified.

S10 Fig. Characterization of *S. meliloti* replicon fusion strains lacking *repC* and *repBC* intergenic region. (A) *repC* deletion constructs pJD202 (Δ*repC1*) and pJD201 (Δ*repC2*) enabled deletion of the megaplasmid *oriV*s in *S. meliloti* strains SmAB and SmABC but not in the wild type. **(B)** Proper deletion in the corresponding strains SmABΔrepC1/2, SmABCΔrepC1/2 and SmABCΔoriV (lacking both *repC1* and *repC2*) was verified via PCR amplification of the deletion site using primers i) 852+853 (wt: 3.15 kb, Δ*repC1*:1.67 kb) and ii) 850+851 (wt: 2.85 kb, Δ*repC2*: 1.39 kb). Additionaly, *repC1/2* deletion in SmABCΔoriV was confirmed using paired-end MiSeq Illumina® sequencing. **C:** Pulsed-field gel electrophoresis (0.5 x TBE, 0.7 % agarose, separation 72 h) banding pattern of PacI-digested gDNA from *S. meliloti* SmAB derivatives (fragments sizes in Mbp: 3.65, 1.67, 0.83, 0.53) and SmABC derivatives (fragment sizes in Mbp: 2.53, 1.94, 1.67, 0.53) verifies the expected genome configuration. M: PFGE marker *S. cerevisiae*, Biorad.

S11 Fig. Marker frequency analysis to assess origin activities and location of replication terminus region in the wild type strain SmCreΔhsdR (A), SmABC (B) and SmABCΔoriV (C). Shown are the averaged copy number profiles based on Illumina sequencing as the log2 ratio of each nucleotide in sequences calculated using a sliding window of 200 bp. Black arrowheads depict the position of individual origin regions (Sibley et al., 2006, Cervantes-Rivera et al., 2011) and terminus regions as predicted by Hendrickson and Lawrence, 2006. Red arrowheads in the profile of SmABCΔoriV represent the deleted *oriA* (Δ*oriA*) and *oriB* (Δ*oriB*) region. Colored (grey, blue, green) arrowheads indicate the local minima of the marker frequency analysis (MFA_{min}) in each strain. Non-filled arrowheads represent the position of the wild type MFA_{min} in profiles of SmABC and SmABCΔoriV.

S12 Fig. Replisome formation and dynamics in SmABCΔR vs SmABCΔoriVΔR. For visualization and comparison of the intracellular replisome dynamics native *dnaN* in MWSm230 (SmABCΔR with *parB::cerulean*) and MWSm285 (SmABCΔoriVΔR with *parB::cerulean*) was replaced by a *dnaN-mCherry* translational fusion using pK19ms DnaN-mCherry. The resulting strains SmABCΔR-DnaN-mCh and SmABCΔoriVΔR-DnaN-mCh were analyzed in a 2 min interval time lapse series. The occurrence of 1-4 mCherry fluorescent foci in SmABCΔR and 1-2 foci in SmABCΔoriVΔR (indicated by white arrowheads) in selected time spots demonstrate a reduced replisome formation for SmABCΔoriVΔR suggesting loss of the replication initiation capacity of the

secondary replicon's *repABC* modules deleted for *repC* and its intrinsic *oriV*. ParB-Cerulean foci visualize the location of the *oriC*(s) over the period of time.

S13 Fig. Generation of antibiotic resistance marker-free *S. meliloti* fusion strains. (A) Deletion of spectinomycin resistance cassette (P_{min2}-*aadA1*) and gentamicin resistance cassette (P_{min2}-*aacC1*) together with the remaining *loxLR* sites from SmAB, SmABC and SmABCΔoriV leads to fusion strain variants SmABΔR, SmABCΔR and SmABCΔoriVΔR**.** i) Proper removal of SpecR in respective strains was realized using construct pJD222 and verified by PCR with primer 792/793 (precursor strains: 2.32 kb, ΔSpecR: 1.16 kb). ii) Construct pJD229 mediated deletion of GmR was confirmed using primer 794/795 (precursor strains: 1.89 kb, ΔGmR: 1.24 kb). **(B)** Genome configuration in SmABΔR, SmABCΔR and SmABCΔoriVΔR was validated using pulsed-field gel electrophoresis (0.5 x TBE, 0.7 % agarose, separation 72 h). Banding pattern of PacI-digested gDNA from SmABΔR (fragments sizes in Mbp: 3.65, 1.67, 0.83, 0.53), SmABCΔR derivative (fragment sizes in Mbp: 2.53, 1.94, 1.67, 0.53) and SmABCΔoriVΔR derivative (fragment sizes in Mbp: 2.53, 1.94, 1.67, 0.53) compared to the direct precursor strains SmAB and SmABC. M: PFGE marker *S. cerevisiae*, Biorad.

S14 Fig. Establishment of a genome architecture independent labeling strategy. (A) Components of the triple color system. A marker free in-frame fusion of *mcerulean* with *parB* (realized by integration of pMW198 via double homologous recombination) enables a constitutively expressed labeling of the chromosomal origin (*oriC)* in all relevant *S. meliloti* genome variants. The second part of the system (FROS) consists of a plasmid-based expression of *lacI-mCherry* and *tetR-mVenus* and enables the labeling of individual positions by genomic integration of related $tetO_{120}$ and $lacO_{120}$ arrays. Equipped with a mobilization site, the pFROS plasmid can be either transferred via conjugation or electroporation in all *S. meliloti* genome variants. **(B)** Validation of suitable ParB-Cerulean function in SmCreΔhsdR (wt), SmABΔR, SmABCΔR and SmABCΔoriVΔR. Snapshot images revealed a formation of either one or two fluorescence foci predominant at the pole envelope indicating the system to constitute as proper *oriC* label. Growth curves of strains with *parB-cerulean* fusion show no negative effect on growth behavior when compared to direct precursor strains. **(C)** Putative *parS* A2+3 boxes for ParB binding on the *S. meliloti* chromosome. An incomplete A2+3 box is located 603 nt upstream of *parA* (*parS1*, gtttcacgtgaaac, position smc3647435), and a further complete palindrome (which is also covered by *parS1*) is situated 2606 nt upstream of *parA* (*parS2*, cgtttcacgtgaaacg, genome position smc3649438). Interestingly, a degenerated variant (*parS3*, gwttcacgtgaawc; w= a or t) exclusively occurs on the chromosome and covers a 90 kb region including *parAB-oriC* (at genome positions smc1945, -54110, -3618431, -3634210, -3647435, -3649439, -3651011, -3652552). **(D)** Fluorescence microscopy analysis of SmCreΔhsdR (wt) and SmABCΔR revealed a sufficient fluorescent signal intensity after 2h, 4h and 6h. This demonstrates that expression of the FROS reporter genes from pFROS can be achieved without any inducer (basal promotor activity coupled to plasmid copy number) over a long period of time which makes the system in particular attractive for long term analysis, like time lapse applications.

S15 Fig. Genome structure validation in SmCreΔhsdR (wt) and SmABCΔR before analysis of spatial DNA organization. Pulsed field electrophoresis banding pattern of PacI-digested gDNA from **(A)** SmCreΔhsdR (wt) and **(B)** SmABCΔR with *parB::cerulean* and integration of either a $tetO_{120}$ array at loci 18, 17, 16, 5 or a $lacO_{120}$ array at loci 2, 3, 10, 13, 6, 15, 14, 9. Fragment sizes of SmCreΔhsdR (wt) derivatives (3.65, 1.35, 1.15, 0.53 Mbp) and SmABCΔR derivatives (2.53, 1.94, 1.67, 0.53 Mbp). Strains SmCreΔhsdR (wt) and SmABCΔR serving as control (C).

S16 Fig. Genome organization in SmABCΔR compared to the wild type. (A) Marker integration sites in genomic DNA of SmABCΔR and SmCreΔhsdR (wt) (for detailed information on the position of genomic integrations please refer to S1 Table) **(B)** Comparison of the fluorescent foci distribution in early G_1-phase cells (cell length max: 2.0 µm, single ParB-Cerulean focus) of in SmCreΔhsdR (wt) and SmABCΔR. Old pole: 1, new pole: -1. Color code: chromosome (grey), pSymA (green), pSymB (blue). Origins are represented as red circles and terminus regions as black diamonds.

S17 Fig. Modeling of spatial DNA arrangement in SmABCΔR. Model prediction for the organization the ABC fusion in SmABC with **(A)** *oriC* **(B)** *oriC* and *terC* **(C)** *oriABC* **(D)** *oriABC* and *terC* as fixpoints at the mean experimental position. Shown are the normalized positions in the cell (old pole: 1; new pole: -1) as a function of the position on the genomic map [Mbp]. Experimental data of origins are indicated by red circles, terminus regions by black diamonds and remaining marker positions with non-filled circles. The red line depicts the model results averaged over 200 cells. Shaded areas represent the standard deviations. For each simulation, a cell size of 1800 nm and a loop size of 1298 bp (DNA within a "blob") was assumed. **E:** Bar chart of the dispersion of the experimental marker data for SmABCΔR. The statistical dispersion is measured via the mean absolute deviation (MAD). The horizontal dashed line indicates the average dispersion (0.35) over all marker.

S18 Fig. Verification of the genome configuration in *S. meliloti* strains with origin and terminus marker. Pulsed-field gel electrophoresis banding pattern of PacI digested gDNA from SmCreΔhsdR (wt), SmABΔR, SmABCΔR and SmABCΔoriVΔR with **(A)** *parB-cerulean* (*oriC*) and $tetO_{120}$ array integration at SMc01205 (*terC*) **(B)** *parB-cerulean* (*oriC*), $tetO_{120}$ array integration at the SMa2383 - SMa2385 intergenic region (*oriA*) and $lacO_{120}$ array integration at the SMb20041 - SMb20042 intergenic region (*oriB*), **(C)** *parB-cerulean* (*oriC*), $tetO_{120}$ array integration at the SMa2383 - SMa2385 intergenic region (*oriA*) and $lacO_{120}$ array integration at SMa1188 (*terA*), **(D)** *parB-cerulean* (*oriC*), $lacO_{120}$ array integration at the SMb20041 - SMb20042 intergenic region (*oriB*) and $tetO_{120}$ array integration at SMb21555 (*terB*). Expected fragment sizes for SmCreΔhsdR derivatives (3.65, 1.35, 1.15,

0.53 Mbp), SmABΔR derivatives (3.65, 1.67, 0.83, 0.53 Mbp), SmABCΔR derivatives (2.53, 1.94, 1.67, 0.53 Mbp) and SmABCΔoriVΔR derivatives (2.53, 1.94, 1.67, 0.53 Mbp). M: PFGE marker *S. cerevisiae*, Biorad.

S19 Fig. Visualization of single cell time lapse data focusing on localization of *oriC*/*oriA*/*oriB* and *oriC*/*terC* regions in SmCreΔhsdR (wt) during the cell cycle. (A) Trajectories of simultaneously tagged *oriC* (ParB-Cerulean), *oriA* (TetR-mVenus) and *oriB* (LacI-mCherry) regions in mother cells (M, upper plots) and daughter cells (D, lower plots). **(B)** Trajectories of *oriC* (ParB-cerulean) and *terC* (TetR-mVenus) regions in M and D-cells. Shown is the relative positions within the cell with old pole at 0 and new pole at 1. Color code: chromosome (grey), pSymA (green), pSymB (blue). Origins are represented as circles and terminus regions as diamonds.

S20 Fig. Visualization of single cell time lapse data focusing on localization of *oriC*/*oriA*/*terA* and *oriC*/*oriB*/*terB* regions in SmCreΔhsdR (wt) during the cell cycle. (A) Trajectories of simultaneously tagged *oriC* (ParB-Cerulean), *oriA* (TetR-mVenus) and *terA* (LacI-mCherry) regions in mother cells (M, upper plots) and daughter cells (D, lower plots). **(B)** Trajectories of *oriC* (ParB-cerulean), *oriB* (LacI-mCherry) and *terB* (TetR-mVenus) regions in M and D-cells. Shown is the relative positions within the cell with old pole at 0 and new pole at 1. Color code: chromosome (grey), pSymA (green), pSymB (blue). Origins are represented as circles and terminus regions as diamonds.

S21 Fig. Visualization of single cell time lapse data focusing on localization of *oriC*/*oriA*/*oriB* and *oriC*/*terC* regions in SmABΔR during the cell cycle. (A) Trajectories of simultaneously tagged *oriC* (ParB-Cerulean), *oriA* (TetR-mVenus) and *oriB* (LacI-mCherry) regions in mother cells (M, upper plots) and daughter cells (D, lower plots). **(B)** Trajectories of *oriC* (ParB-cerulean) and *terC* (TetR-mVenus) regions in M and D-cells. Shown is the relative positions within the cell with old pole at 0 and new pole at 1. Color code: chromosome (grey), pSymA (green), pSymB (blue). Origins are represented as circles and terminus regions as diamonds.

S22 Fig. Visualization of single cell time lapse data focusing on localization of *oriC*/*oriA*/*terA* and *oriC*/*oriB*/*terB* regions in SmABΔR during the cell cycle. (A) Trajectories of simultaneously tagged *oriC* (ParB-Cerulean), *oriA* (TetR-mVenus) and *terA* (LacI-mCherry) regions in mother cells (M, upper plots) and daughter cells (D, lower plots). **(B)** Trajectories of *oriC* (ParB-cerulean), *oriB* (LacI-mCherry) and *terB* (TetR-mVenus) regions in M and D-cells. Shown is the relative positions within the cell with old pole at 0 and new pole at 1. Color code: chromosome (grey), pSymA (green), pSymB (blue). Origins are represented as circles and terminus regions as diamonds.

S23 Fig. Visualization of single cell time lapse data focusing on localization of *oriC*/*oriA*/*oriB* and *oriC*/*terC* regions in SmABCΔR during the cell cycle. (A) Trajectories of simultaneously tagged *oriC* (ParB-Cerulean), *oriA* (TetR-mVenus) and *oriB* (LacI-mCherry) regions in mother cells (M, upper plots) and daughter cells (D, lower plots). **(B)** Trajectories of *oriC* (ParB-cerulean) and *terC* (TetR-mVenus) regions in M and D-cells. Shown is the relative positions within the cell with old pole at 0 and new pole at 1. Color code: chromosome (grey), pSymA (green), pSymB (blue). Origins are represented as circles and terminus regions as diamonds.

S24 Fig. Visualization of single cell time lapse data focusing on localization of *oriC*/*oriA*/*terA* and *oriC*/*oriB*/*terB* regions in SmABCΔR during the cell cycle. (A) Trajectories of simultaneously tagged *oriC* (ParB-Cerulean), *oriA* (TetR-mVenus) and *terA* (LacI-mCherry) regions in mother cells (M, upper plots) and daughter cells (D, lower plots). **(B)** Trajectories of *oriC* (ParB-cerulean), *oriB* (LacI-mCherry) and *terB* (TetR-mVenus) regions in M and D-cells. Shown is the relative positions within the cell with old pole at 0 and new pole at 1. Color code: chromosome (grey), pSymA (green), pSymB (blue). Origins are represented as circles and terminus regions as diamonds.

S25 Fig. Visualization of single cell time lapse data focusing on localization of *oriC*/Δ*oriA*/Δ*oriB* and *oriC*/*terC* regions in SmABCΔoriVΔR during the cell cycle. (A) Trajectories of simultaneously tagged *oriC* (ParB-Cerulean), Δ*oriA* (TetR-mVenus) and Δ*oriB* (LacI-mCherry) regions in mother cells (M, upper plots) and daughter cells (D, lower plots). **(B)** Trajectories of *oriC* (ParB-cerulean) and *terC* (TetR-mVenus) regions in M and D-cells. Shown is the relative positions within the cell with old pole at 0 and new pole at 1. Color code: chromosome (grey), pSymA (green), pSymB (blue). Origins are represented as circles and terminus regions as diamonds.

S26 Fig. Visualization of single cell time lapse data focusing on localization of *oriC*/Δ*oriA*/*terA* and *oriC*/Δ*oriB*/*terB* regions in SmABCΔoriVΔR during the cell cycle. (A) Trajectories of simultaneously tagged *oriC* (ParB-Cerulean), Δ*oriA* (TetR-mVenus) and *terA* (LacI-mCherry) regions in mother cells (M, upper plots) and daughter cells (D, lower plots). **(B)** Trajectories of *oriC* (ParB-cerulean), Δ*oriB* (LacI-mCherry) and *terB* (TetR-mVenus) regions in M and D-cells. Shown is the relative positions within the cell with old pole at 0 and new pole at 1. Color code: chromosome (grey), pSymA (green), pSymB (blue). Origins are represented as circles and terminus regions as diamonds.

S27 Fig. Timepoint of visual segregation of origin and terminus foci in SmCreΔhsdR (wt), SmAB (AB), SmABC (ABC) and SmABCΔoriVΔR (ABCΔ) daughter cells [D]. Bar chart depicting the timepoint of visual foci segregation within the *S. meliloti*

cell cycle normalized to 100 % (0 % - cell cycle start, 100 % - cell cycle completed). Bars are indicative for the standard deviation (SD) with the mean as black centered lines.

S28 Fig. Localization of origin and terminus foci segregation in SmCreΔhsdR (wt), SmAB (AB), SmABC (ABC) and SmABCΔoriVΔR (ABCΔ) daughter cells [D]. Bar chart depicting the longitudinal position of visual foci segregation within the *S. meliloti* cell normalized to 1 (0 - old pole, 1 – new pole). Bars are indicative for the standard deviation (SD) with the mean as black centered lines.

S29 Fig. *oriA* and *oriB* segregation. (A) Scatter plot with timing of the *oriA* and *oriB* segregation events post *oriC* segregation in the SmCreΔhsdR (wild type), SmABΔR (AB), SmABCΔR (ABC) and SmABCΔoriVΔR (ABCΔ) subdivided in mother and dauther cells (n=100 each). Black line depict the mean values of the plot data. **(B)** Microscopy images of cells with simultaneously segregating *oriA/ΔoriA* and *oriB/ΔoriB* foci within the chosen time lapse settings (5 minutes intervals between the individual images). Arrowheads depict the localization of *oriA/ΔoriA* (yellow) and *oriB/ΔoriB* (red) before (upper panel) and after (lower panel) the segregation event. Scale bar: 1 µm. **C:** Percentage of cells per strain (n=200 each) with simultaneous and consecutive occurring segregation event.

S30 Fig. Comparison of *oriC*, *oriA/ΔoriA* and *oriB/ΔoriB* distribution in SmCreΔhsdR (wt), SmABΔR, SmABCΔR and SmABCΔoriVΔR. Violin plots depicts the normalized distance of the individual origin regions to the cell center (cell poles: 1 and -1, cell center: 0). Plots are based on snapshot analysis of G_1-phase cells filtered by size with a cut-off of 2.0 µm. Wild type (n=639), SmABΔR (n=460), SmABCΔR (n=405) and SmABCΔoriVΔR (n=246).

S31 Fig. Origin co-localization scheme for SmCreΔhsdR (wt), SmABΔR, SmABCΔR and SmABCΔoriVΔR. The scheme depict the distribution pattern of *oriA/ΔoriA* (green spots) *oriB*/Δ*oriB* (blue spots) and *oriC* (grey spots) in relation to each other. Therefore, cells were divided into four compartments (1 to 0.5, 0.5 to 0, 0 to -0.5 and -0.5 to -1). Cells analyzed: SmCreΔhsdR (wt) (n=639), SmABΔR (n=460), SmABCΔR (n=405) and SmABCΔoriVΔR (n=246).

S32 Fig. *oriC* localization pattern in SmABCΔoriVΔR cells after one cell-division cycle. Depicted are the percentage of the predominant *oriC* positions in the next generation of sibling cells emerging from either sibling 1 (grey) or sibling 2 (white). Cells analyzed: n=80.

S33 Fig. Analysis of CckA^{R436H} in *S. meliloti* wild type and genome fusion strains. (A) Schematic illustration of functional domains of CckA predicted by Pfam, COG and SMART via NCBI CDD (Marchler-Bauer et al., 2011, 2015 and 1017). The red line depicts the position of the missense mutation R436H. **(B)** Densitiy map of *oriC* (ParB-cerulean) localization in predivisional sibling cells of SmCreΔhsdR (wt) and SmABCΔR with original and mutagenized *cckA*. **(C)** Percentage of predividional sibling cells of SmCreΔhsdR (wt) and SmABCΔR with either both *oriCs* located at the poles (lower picture and values) or with at least one *oriC* focus located in the midcell area (upper picture and values). **(D)** Growth curves of SmCreΔhsdR (wt) and SmABCΔR with original CckA compared to the respective strains with CckA^{R436H}. **(E)** Growth comparison of SmABCΔoriVΔR with the precursor strain SmABCΔoriV and SmABCΔoriVΔR with *parB::cerulean* fusion.

S1 Table. Underlying data of S16B Fig. Mean and standard deviation (SD) of the relative longitudinal positions of fluorescent foci within analyzed cells of SmABCΔR and the wild type. Old cell pole at 1, new cell pole at -1.

S2 Table. Timepoint of origin and terminus foci segregation in SmCreΔhsdR (wt), SmABΔR, SmABCΔR and SmABCΔoriVΔR mother cells [M]. Corresponding values to Fig.5A (main manuscript). Mean and standard deviation (SD) of corresponding origin / *repABΔC* (Δ*oriA* or Δ*oriB*) and terminus foci segregation normalized to a cell cycle duration of 100 % (0 % - cell cycle start, 100 % - cell cycle completed) in cells analyzed (n).

S3 Table. Localization of origin and terminus foci segregation in SmCreΔhsdR (wt), SmAB, SmABC and SmABCΔoriVΔR mother cells [M]. Corresponding values to Fig.5B. Mean and standard deviation (SD) of the relative longitudinal position of corresponding origin/ *repABΔC* (Δ*oriA* or Δ*oriB*) and terminus foci segregation normalized to 1 (0 - old pole (OP), 1 - new pole (NP)) within cells analyzed (n).

S4 Table. Values corresponding to S27 Fig. Mean and standard deviation (SD) of origin / *repABΔC* (Δ*oriA* or Δ*oriB*) and terminus foci segregation normalized to a cell cycle duration of 100 % (0 % - cell cycle start, 100 % - cell cycle completed) in cells analyzed (n).

S5 Table. Values corresponding to S28 Fig. Mean and standard deviation (SD) of the relative longitudinal position of corresponding origin/ *repABΔC* (Δ*oriA* or Δ*oriB*) and terminus foci segregation normalized to 1 (0 - old pole, 1 - new pole) within cells analyzed (n).

S6 Table. Coding sequences that were removed or truncated upon the replicon fusion procedure. For details on the individual fusion site (FS) please refer to S1 Fig and S2 Fig.

S7 Table. Single nucleotide variations associated with the fusion procedure. Reference positions refer to the genome of *S. meliloti* SmCreΔhsdR which was used as the reference for the basic variant detection analysis. CDS: coding sequence, * paralogue, MBOAT: membrane bound O-acyl transferase

S8 Table. Single nucleotide variations and nucleotide deletions in *S. meliloti* genome fusion strains. Reference positions refer to the genome of *S. meliloti* SmCreΔhsdR which was used as the reference for the basic variant detection analysis. Red highlighted row represents the SNV which lead to the missense mutation R436H in CckA (S33 Fig). CDS: coding sequence, IGR: intergenic region.

S9 Table. Bacterial strains used in this study.

S10 Table. Plasmids used in this study.

S11 Table. Construction of *S. meliloti* replicon fusion strains and derivatives.

S12 Table. Plasmid construction.

S13 Table. Oligonucleotides used in this study.

S1 Text. Model of compacted DNA.

S2 Text. Monte Carlo sampling of configuration space.

S3 Text. SI References.